UC Berkeley
UC Berkeley Electronic Theses and Dissertations

Title
Dynamics of the IFT Machinery at the Ciliary Tip

Permalink
https://escholarship.org/uc/item/6hz1m8vn

Author
Chien, Alexander

Publication Date
2019

Supplemental Material
https://escholarship.org/uc/item/6hz1m8vn#supplemental

Peer reviewed|Thesis/dissertation

Dynamics of the IFT Machinery at the Ciliary Tip

By

Alexander Chien

A dissertation submitted in partial satisfaction of the

requirements for the degree of

Doctor of Philosophy

in

Biophysics

in the

Graduate Division

of the

University of California, Berkeley

Committee in charge:

Professor Ahmet Yildiz, Chair
Professor David Drubin
Professor Roberto Zoncu
Professor Krishna Niyogi

Spring 2019

Abstract

Dynamics of the IFT Machinery at the Ciliary Tip

By

Alexander Chien

Doctor of Philosophy in Biophysics

University of California, Berkeley

Professor Ahmet Yildiz, Chair

Intraflagellar transport (IFT) is essential for the elongation and maintenance of eukaryotic cilia and flagella. Due to the traffic jam of multiple trains at the ciliary tip, how IFT trains are remodeled in these turnaround zones cannot be determined by conventional imaging. Using PhotoGate, I visualized the full range of movement of single IFT trains and motors in *Chlamydomonas* flagella. I observed that anterograde trains split apart and IFT complexes mix with each other at the tip to assemble retrograde trains. Dynein-1b is carried to the tip by kinesin-II as inactive cargo on anterograde trains. Unlike dynein-1b, kinesin-II detaches from IFT trains at the tip and diffuses in flagella. As the flagellum grows longer, diffusion delays return of kinesin-II to the basal body, depleting kinesin-II available for anterograde transport. These results suggest that dissociation of kinesin-II from IFT trains serves as a negative feedback mechanism that facilitates flagellar length control in *Chlamydomonas*.

Introduction to the dissertation

After joining the Ahmet Yildiz lab in 2014, I took over the Intraflagellar Transport (IFT) project from Sheng-Min Shih, a former graduate student of Ahmet's. Sheng-Min had used an early incarnation of the PhotoGate, a photobleaching technique created in the Yildiz lab, to observe the dynamics of IFT proteins and kinesin-2 in *Chlamydomonas*, a green algae. When I took over the project, the lab had developed a new method of doing PhotoGate experiments that was more precise and induced less photobleaching and photodamage in cells. I adapted this new method for use on *Chlamydomonas* by making improvements to the control software and instrumentation. I used these improvements to perform PhotoGate experiments on the IFT motor dynein-1b and observed its tip dynamics. I analyzed how dynein-1b transitioned from anterograde to retrograde transport. To study the interaction of the two IFT motors, kinesin-2 and dynein-1b, I worked with Mary Porter from the University of Minnesota to generate new strains of *Chlamydomonas* which had both dynein and kinesin fluorescently tagged. This strain allowed me to directly visualize that dynein-1b is carried to the flagellar tip as an inactive passenger of kinesin-2. At the tip, kinesin-2 detaches from IFT trains and diffuses within the flagellum. This allowed me to propose a new model for motor protein teamwork in IFT. Next, I explored the connections between our recent discovery of kinesin-2's retrograde diffusion and the open question of how *Chlamydomonas* controls the length of its flagella. Using a combination of cell imaging and numerical modeling, I showed that kinesin-2's slow diffusive return could cause it to become a limiting factor of IFT in long flagella. Because IFT sets the rate of flagellar growth, I proposed that diffusion of kinesin-2 can serve as a negative feedback mechanism to limit the flagellar growth.

Dedication

Above all, I thank my parents, Te-Yen Chien and Shu-Chean Chien, for their love and support of my endeavors. I try to live to their example and hope to make them proud.

I'm lucky to have friends from every stage of my life who have kept me smiling and optimistic for the future. I hope to always do the same for them.

I could have not asked for a better group of co-workers, mentors, and friends than the Ahmet Yildiz Lab. Each person here is uniquely inspiring.

Table of Contents:

Chapter 1: Introduction

Cilia (or eukaryotic flagella, terms essentially referring to the same organelle) are hair-like organelles that extend from the plasma membrane of nearly all mammalian cells. The core structural component of a cilium is the axoneme, a ring of nine unipolar doublet microtubules surrounding a central pair of singlet microtubules. Cilia play essential roles in cell motility, generate the movement of fluids over multiciliated surfaces, and sense extracellular signals (Satir et al., 2010). To assemble and maintain functional cilia, the IFT machinery (Kozminski et al., 1993) transports axonemal precursors and sensory proteins bidirectionally between the cell body and the ciliary tip. Defects in IFT are linked to a wide range of human diseases including Bardet-Biedl syndrome, retinal degeneration, and polycystic kidney disease (Brown and Witman, 2014).

Intraflagellar cargoes interact with multiprotein complexes known as IFT particles that are organized into larger IFT trains as they enter the flagellum (Cole et al., 1998; Lechtreck et al., 2017; Pigino et al., 2009). In most species, the IFT trains are transported anterogradely from the base to the tip of a flagellum by heterotrimeric kinesin-II (Kozminski et al., 1995), but some species also use a second homodimeric kinesin to build more specialized sensory cilia (Snow et al., 2004). Once the trains reach the tip, they are reorganized and transported retrogradely to the ciliary base by dynein-1b (Pazour et al., 1999; Porter et al., 1999; Signor et al., 1999). Along the length of a cilium, the activities of kinesin and dynein motors are reciprocally coordinated, such that only one type of a motor is active at a time (Shih et al., 2013). As a result, trains move between the tip and base of the cilium without significant pauses or back-and-forth motion (Dentler, 2005; Engel et al., 2009) and switch directions at the turnaround zones (Ishikawa and Marshall, 2011; Laib et al., 2009; Shih et al., 2013). Dynein-1b requires kinesin-II activity to reach the ciliary tip, suggesting that it travels as an inactive passenger on anterograde trains (Iomini et al., 2001; Pedersen et al., 2006; Rompolas et al., 2007). Because anterograde and retrograde IFT trains have different sizes and depart at different frequencies (Dentler, 2005; Iomini et al., 2001), IFT trains must be remodeled at the distal tip and the flagellar base.

The mechanism underlying the remodeling of IFT complexes at the ciliary tip and base cannot be directly observed by conventional microscopy methods because multiple trains coexist in these turnaround zones (Buisson et al., 2013; Iomini et al., 2001; Wren et al., 2013). In this work, we adapted PhotoGate (Belyy et al., 2017) to control the number of fluorescent IFT trains entering the flagellum of the unicellular algae *Chlamydomonas reinhardtii*. Using this approach, we monitored the turnaround behavior and remodeling of single IFT trains at the flagellar tip. We also elucidated the mechanisms by which the kinesin and dynein motors are recycled in this process and IFT trains reverse their direction of motion. The dynamics of IFT motor turnover at the tip suggest a new mechanism for how *Chlamydomonas* controls the length of its flagella at steady state.

1

Background:
Eukaryotic Flagella
Cilia and flagella (which are essentially the same organelle) are linear, protruding organelles displayed on the surface of most eukaryotic cell types. As the name suggests, their structure can be described as whiplike, a comparison which is apt considering how many types undulate in wave-like motions to create or respond to fluid flows. Many bacterial cells express one or more motile whiplike appendages made of the protein flagellin that help generate movement. These structures are also known as flagella; however, they are structurally, functionally, and evolutionarily much different from those in eukaryotic cells, and the fact that the two structures share a name is a confusing etymological artefact. In this thesis, I will use "flagella" and "cilia" interchangeably, and they will refer specifically to the eukaryotic organelle.

Flagella have myriad cellular functions. In humans, motile cilia in the airway epithelium beat to create fluid flows that move debris and mucous out of the respiratory tract. Additional types of motile cilia are found in the oviduct and spermatozoa. Many cell types express multiple motile cilia on the surface of their plasma membrane; additionally, almost all cell types can also express a single non-motile primary cilium. Because it doesn't move, the primary cilium was once considered a vestigial organelle. Nowadays, it is recognized as a cellular antenna which is involved in various signaling pathways such as Hedgehog. Specialized sensory cilia also exist and are found in retinal neurons or the olfactory epithelium. As such, it is not surprising that cilia are necessary cellular structures in mammals and their absence is lethal (Nachury and Mick, 2019).

A popular model organism for flagellar research is *Chlamydomonas reinhardtii*, a green algae that is also used for studying photosynthesis, cell-cell recognition, light response, and cellular movement. *Chlamydomonas* is a unicellular photosynthetic eukaryote with a football-shaped body and two long flagella located at one end of the cell (Figure 1.1). In its primary mode of movement, the cell beats its flagella in a breaststroke motion to swim through its low Reynolds number environment (Silflow and Lefebvre, 2011). They can also "glide" along surfaces like glass coverslips, being pulled by their flagellum (Shih et al., 2013). *Chlamydomonas* flagella, similar to their mammalian counterparts, have signal transduction capabilities: they can act as mechanosensors for an "avoiding response" upon swimming into obstacles (Fujiu et al., 2011) and they relay signals for cell-cell fusion and progression through the mating pathway when two gametes meet (Silflow and Lefebvre, 2011).

Figure 1.1. Electron microscopy image of *Chlamydomonas reinhardtii*. From the Dartmouth Electron Microscopy Facility.

Chlamydomonas is a well-studied model organism for flagellar research for several reasons. It can be grown easily in large amounts, and its cell cycle can be synchronized by alternating light-dark conditions. Its flagella can be easily isolated from the cell bodies in large amounts for biochemical analysis. Mutagenesis studies have produced many mutant strains that can be screened for flagellar defects in motility or visual structure, and they can be crossed with each other easily to combine mutations. Its swimming behavior is regular and responsive to various light or chemical stimuli. *Chlamydomonas* can survive without its flagella, allowing for more in-depth perturbations of the system, and they regrow their flagella in one hour after deflagellation. Finally, when at rest, the cells lay with the flagella flattened upon glass coverslides, allowing for facile observation (Morga and Bastin, 2013).

Flagellar structure
The core of the flagellum is a tubulin-based structure called the axoneme. In *Chlamydomonas*, the bulk of the axoneme is composed of a ring of nine microtubule doublets, a structure in which 13 microtubule protofilaments form a ring (the A-tubule) and are joined by 10 additional protofilaments in a loop structure (the B-tubule). At the very base of the flagellum, in the basal body, the axoneme is seeded by triplet microtubules (the C-tubule) rather than doublets. Conversely, at the flagellar tip, the doublet microtubules give way to single microtubules. In motile cilia like those in *Chlamydomonas*, a central pair of microtubules through the center of the microtubule doublet ring extends to the tip of the flagellum. As such, most motile cilia are designated as having a "9+2" configuration. Non-motile primary cilia lack the central pair and are designated as having a "9+0" configuration (Viswanadha et al., 2017).

Along the length of the flagellum, microtubules are interconnected radially by radial spoke proteins which span from the central pair microtubules to the outer doublet microtubules. These are T-shaped protein complexes that repeat every 96 nm along the length of the flagellum,

3

stabilizing the ring structure along its length. Radial spokes contain at least 23 unique polypeptides, with both structural and signaling capacities. *Chlamydomonas* strains with radial spoke mutations often have ciliary structure and motility defects. Structural, genetic, and motility studies of these mutants suggest that the radial spokes transmit mechanical and/or mechanochemical signals from the central pair of microtubules to structures on the outer doublets (Yang et al. 2006).

The swimming motion of motile cilia such as those in *Chlamydomonas* is powered by inner and outer dynein arm motor proteins. Outer dynein arms are arranged every 24 nm along the outer microtubule doublets and are composed of alpha, beta, and gamma subunits. These proteins provide much of the power for flagellar movement and regulate the flagellar beating frequency. Inner dynein arms are varied and have more variable localization on the 96 nm axonemal repeat. These motors control the shape of ciliary bending in both inward and outward directions (Viswanadha et al., 2017).

The flagellar membrane is contiguous with the rest of the cell membrane, but has a unique membrane protein composition because of a membrane diffusion barrier located at the base of the flagellum. This allows the flagellar membrane to be enriched in various structural and signaling receptor proteins, allowing it to participate in signal transduction, chemosensation, and mechanoreceptor roles. Many transducers in the well-studied Hedgehog signaling pathway are localized to the flagellum at different stages of signaling. Photoreceptor cells in the retina are enriched in rhodopsins that allow them to act as light-activated antennae. *Chlamydomonas* gametes' flagella interact during the mating process to initiate signaling cascades ultimately resulting in cell-cell fusion (Bloodgood, 2012). Moreover, flagellar membrane glycoproteins allow *Chlamydomonas* to adhere and exert forces on surfaces during gliding motility (Shih et al. 2013).

The base of the flagellum is a unique hub at the intersection of the flagellar lumen and the cell's cytoplasm (Dutcher et al. 2016). The basal body is a ring structure at the foot of the flagellum based upon the triplet microtubules of a centriole. These triplet microtubules, termed A, B, and C, give rise to the outer doublets (A and B) of the flagellum. Between the basal body and the cilium is the transition zone, in which transition fibers serve as a diffusion barrier limiting entry to the flagellar lumen, and anchor the basal body to the plasma membrane. Further, Y-linker proteins connect the microtubule core to the ciliary membrane.

Intraflagellar Transport

The flagellum is a dynamic organelle; it is resorbed into the cell prior to mitosis and grown again after cell division. Pioneering work in *Chlamydomonas* showed that the flagellum is built continuously, being lengthened when new flagellar material is deposited at its distal tip. Moreover, as it grows to lengths of several microns or longer, the site of assembly moves further away from the cell body. Protein synthesis does not occur within the flagellum, as ribosomes cannot penetrate the diffusion barrier at the flagellar base. This diffusion barrier also prevents larger flagellar proteins from entering through passive mechanisms. Even if such a barrier did not exist, passive diffusion along a linear, microns-long organelle would be an inefficient method for

concentrating flagellar building blocks at the site of assembly at the end of the flagellum.

To address this issue, cells employ intraflagellar transport (IFT), a microtubule-motor-based cargo transport mechanism (Figure 1.2). IFT was first observed using DIC microscopy as diffraction-limited bulges moving processively along the full length of *Chlamydomonas* flagella, and has since been observed in most ciliated organisms. Transport moving toward the tip was named "anterograde transport" and transport moving from the tip toward the base was named "retrograde." Later electron microscopy studies showed that these IFT "trains" formed linear, electron-dense, repetitive arrays between the microtubule axoneme and the ciliary membrane, with lengths ranging from 250 nm to 750 nm. Anterograde trains move at approximately 2 μm/s, while retrograde trains move at 3 μm/s. The frequency of IFT trains is measured to be approximately 1Hz in both directions, though several studies reported that retrograde IFT is more frequent than anterograde IFT (Dentler, 2005; Engel et al., 2009; Iomini et al., 2001; Kozminski et al., 1993; Qin et al., 2007; Shih et al., 2013).

Anterograde IFT has been found to be dependent on the motor protein kinesin-2, which walks toward the plus-end of microtubules. Cells with kinesin-2 defects fail to assemble flagella, and inactivation of a temperature-sensitive mutant of kinesin-2 causes IFT to abruptly cease and flagella to resorb slowly back to the cell body (Kozminski et al., 1995). Retrograde IFT is dependent on dynein-1b, a motor which walks toward the minus-end of microtubules. When dynein-1b is abruptly inactivated in temperature-sensitive strains, cells develop defects in which the flagellum swells with IFT train protein which move in through anterograde transport but cannot leave via retrograde movement. Cells harboring mutations in which dynein-1b is defective often fail to assemble cilia (Pazour et al. 1998; Porter et al. 1999; Siggnor et al., 1999).

Experiments using the temperature-sensitive mutant which abrogates IFT at high "restrictive" temperatures showed that these trains consisted of repetitive units of a 22+ subunit protein complex. IFT complexes co-purify in two sub-complexes, named IFT A (6 proteins) and IFT B (16 proteins). IFT B can be further divided into IFT B1 and IFT B2. IFT B proteins are necessary for anterograde transport based on the fact that IFT B mutant strains often fail to assemble flagella. Conversely, IFT A is thought to be associated with dynein and retrograde transport because mutations in these proteins still allow for ciliogenesis, but lead to abnormally-bulged flagella with high amounts of IFT B complex proteins (Taschner and Lorentzen, 2016).

IFT complexes co-immunoprecipitate with structural flagellar proteins and membrane receptors, suggesting that they are carried as cargo by the transport machinery and deposited at the end of the flagellum. Examples of these proteins are tubulin, flagellar dyneins, and radial spoke proteins (Prevo et al. 2017). Cargos such as tubulin and dynein regulatory complex proteins are transported to the flagellar tip by IFT trains. After arrival at the tip, these cargos diffuse briefly before settling in place, presumably being incorporated into the flagellar structure.
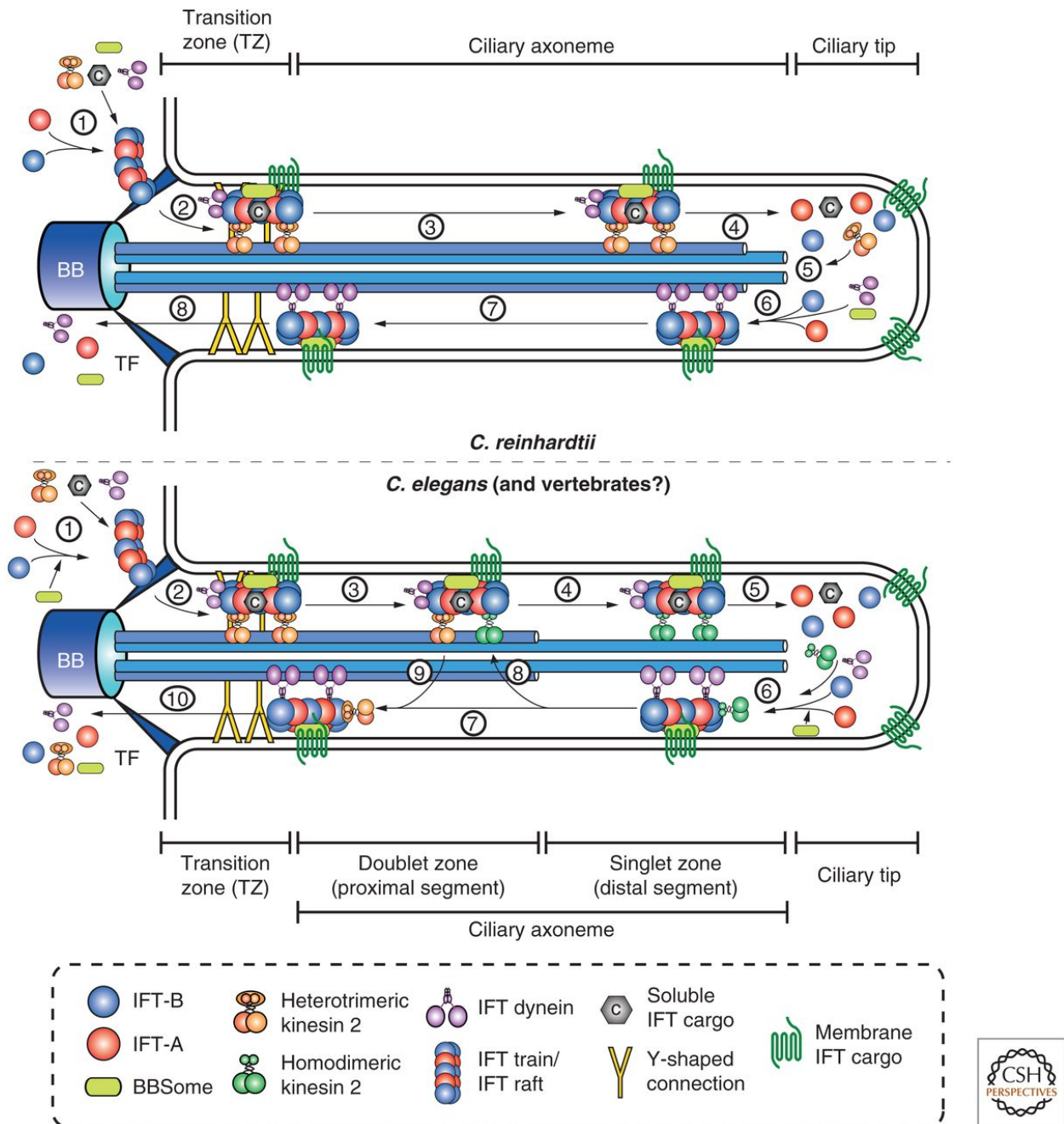
Figure 1.2. Schematic of Intraflagellar Transport in multiple model systems. From Taschner and Lorentzen, 2016.

**Flagellar length control in *Chlamydomonas***

Chlamydomonas' flagellum is an excellent system for studying a basic question in biology: how does a cell regulate the size of its organelles? Within a population of *Chlamydomonas* cells, the flagellar length is tightly regulated, approximately 10-12 microns in wild-type cells. Moreover, the flagellum is a dynamically maintained organelle. As mentioned before, the flagellum actively resorbs before cell division and grows out again afterwards. Additionally, *Chlamydomonas* can

actively shed its flagella in response to environmental stresses such as shear forces and acidic environments. Upon return to favorable conditions, wild-type cells will regrow their flagella to full length in approximately 90 minutes. This process occurs with decelerating kinetics: when flagella are short, they grow very quickly. The growth rate decreases as the flagella grow longer (Figure 1.3, Rosenbaum et al., 1969).
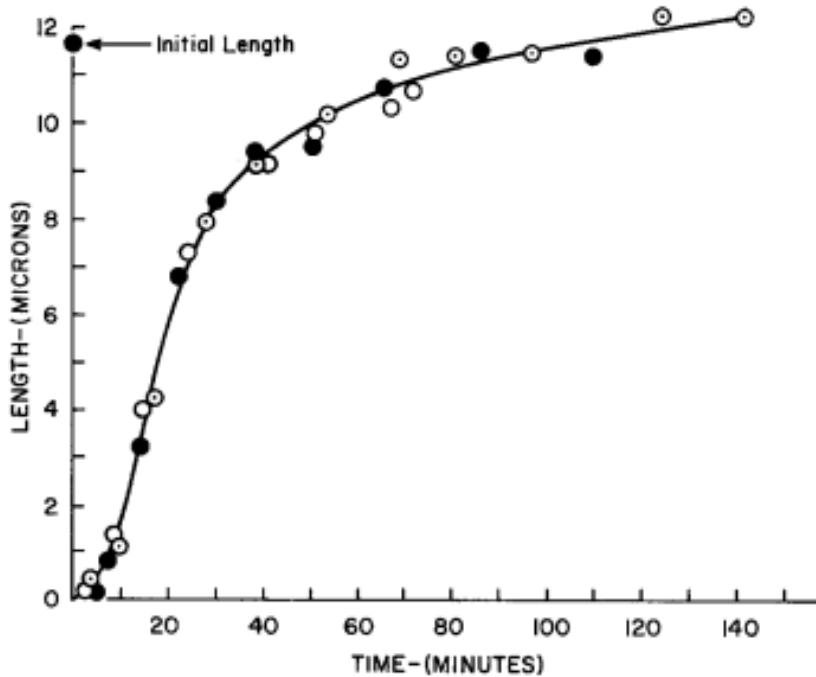
Figure 1.3. The classic flagellar growth curve after deflagellation at time 0. From Rosenbaum et al., 1969.

Because the flagellum is a dynamic organelle, its growth is balanced by disassembly. Flagellar disassembly is a relatively poorly understood process. Early experiments observed that after IFT is halted in a temperature-sensitive kinesin mutant the flagella slowly decrease in size, with protein continually being lost from the flagellar tip. This shrinkage rate was constant for all lengths of flagella. As such, flagellar length control can be viewed in terms of a Balance-Point Model (Marshall and Rosenbaum, 2001) in which an assembly rate which changes with flagellar length competes against a length-independent disassembly rate. The equilibrium length of the flagellum is set when the two rates become equal (Figure 1.4, Marshall et al., 2005).
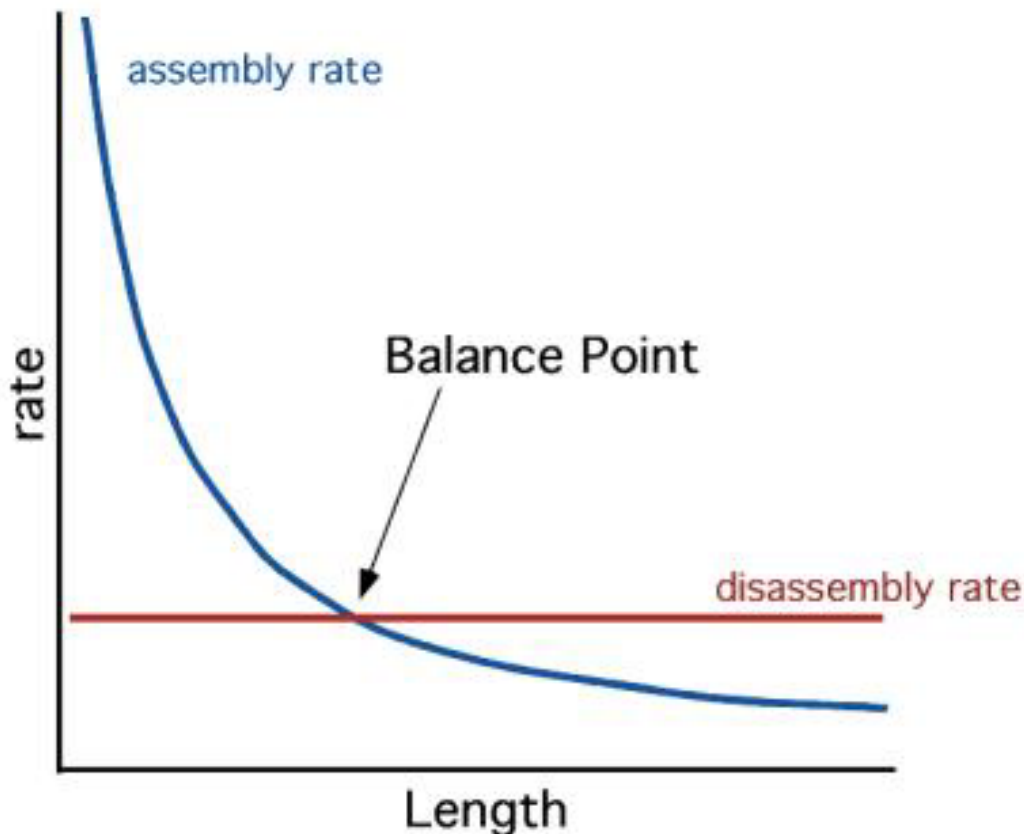
Figure 1.4. A representation of the Balance Point Model of flagellar length control. From Marshall et al., 2005.

Flagellar growth is likely regulated at many different levels. After deflagellation, cells upregulate the production of many flagellar proteins in order to meet the demands of building a new organelle. When protein synthesis is blocked via the drug cycloheximide, cells grow half-length flagella, suggesting that some pool of flagellar components is constitutively available in the cell body even when flagella are already present. Signaling pathways no doubt play a role: mutations in various kinases and phosphatases are known to lead to phenotypes of excessively long or short flagella. Cells treated with lithium, a GSK3 kinase inhibitor, grow flagella that are 50% longer than normal (Nakamura et al., 1987).

Several studies also suggested that IFT also plays a role in the determining assembly rate and equilibrium length of the flagella. Fluorescence experiments have shown that loading of cargos onto IFT trains is highly correlated with flagellar growth: IFT trains are much more highly laden with proteins like tubulin and structural proteins while the flagellum is in its rapid growth phase. Interestingly, the frequency and speed of IFT trains vary only slightly as flagella grow longer. Instead, IFT trains are significantly larger and powered by more kinesin-2 when flagella are short and experiencing rapid growth (Figure 1.5, Engel et al., 2009). Presumably, this is to allow for more cargo loading on trains.
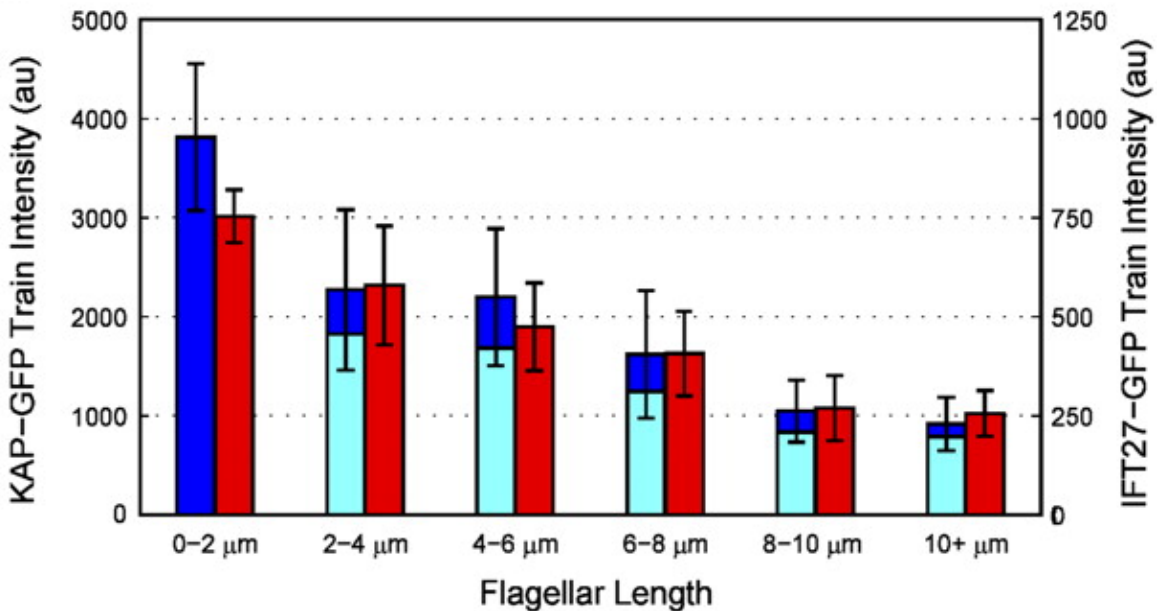
Figure 1.5. The amount of kinesin (blue) and IFT protein (red) on IFT trains in flagella of various lengths. From Engel et al., 2009.

Imaging the Dynamics of IFT Components in Live *Chlamydomonas* Cells

One of the advantages of studying IFT in *Chlamydomonas* is that these cells have 2 long flagella that lie flat on glass coverslips. Therefore, whole flagella can easily be viewed in a single plane of focus. Moreover, many mutant strains exist in which IFT proteins, motors, and cargo are labeled with fluorescent proteins. Because flagella have a diameter of approximately 200 nm, the entire organelle can be neatly imaged in the evanescent field of a Total Internal Reflection Fluorescence (TIRF) microscope. Because the flagella are linear structures, the entire fluorescence activity of the organelle can be captured in a 2 dimensional kymograph (position vs. time plot over a linear region).

The IFT field has benefitted greatly from real-time TIRF imaging of fluorescently-tagged IFT complexes. In a conventional kymograph of IFT proteins moving in a flagellum, moving IFT complexes appear as diagonal lines because they move at constant speeds, seldom pause, and never change direction except at the ciliary tip. The slope of the lines in a kymograph give us information about a train's speed, while their spacing gives us information about their frequency. The loading of the fluorescent protein can be deduced by the intensity of the fluorescent signal in the image.

Imaging the dynamics of IFT particles at the flagellar tip, however, becomes challenging. In this small region, multiple anterograde IFT trains enter at the same time as other retrograde IFT trains leave. Additionally, a small pool of IFT proteins resides at the flagellar tip at a time, presumably because of a time delay in the tip turnover process. As such, under normal TIRF imaging conditions, there is a traffic jam at the flagellar tip and it is impossible to determine the fate of proteins from individual IFT trains once they enter the flagellar tip.

9

To get around this problem, we adapted the PhotoGate, a photobleaching technique developed in the Yildiz lab, to IFT in *Chlamydomonas*. PhotoGate is similar to Fluorescence Recovery After Photobleaching (FRAP) in that a region of interest in a cell is selectively photobleached. However, unlike FRAP, additional photobleaching steps occur at the periphery of this region to carefully control the recovery of fluorescence into the region (Figure 1.6, Belyy et al., 2017).

In the PhotoGate's original incarnation, a focused laser "gate" beam is swept through a circular region to photobleach fluorescent molecules. The beam is then turned off to allow unbleached molecules to diffuse into the area at a low concentration. To prevent other unbleached diffusing molecules from clouding the field of view, the gate beam is continuously activated. This allows the movement of individual proteins to be unambiguously tracked for long periods of time (Figure 1.6, Belyy et al., 2017).
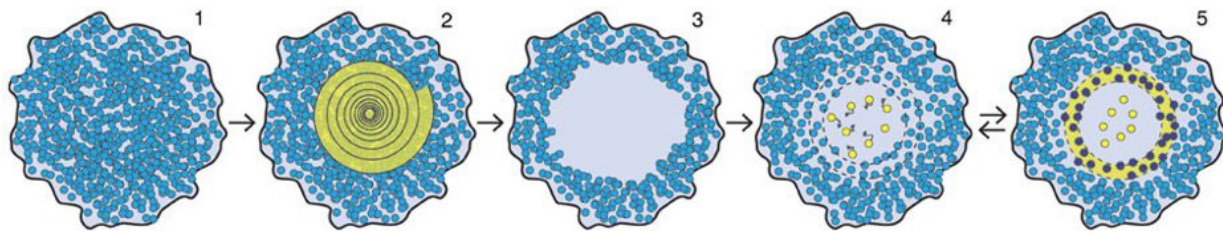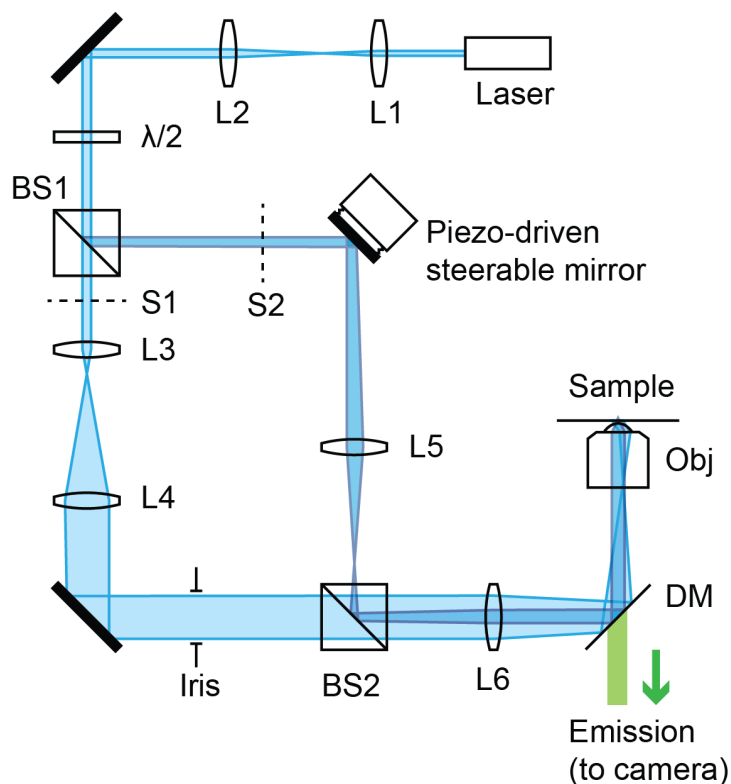

Figure 1.6. Image from "PhotoGate microscopy to track single molecules in crowded environments," From Belyy et al., 2017.

To study the dynamics of individual intraflagellar transport trains, we modified the PhotoGate to operate on a linear region rather than a circular one. For *Chlamydomonas* experiments, all fluorescence in the flagellum is photobleached by moving the gate beam along the length of the flagellum. Next, the gate beam is turned off to allow a single anterograde train into the photobleached area. The gate beam is re-activated in place to bleach all trains following the unbleached anterograde train. This allows us to view the complete trajectory of proteins from a single anterograde train as they move to the tip of the flagellum, remodel to retrograde movement, and begin returning to the cell body (Figure 1.7).
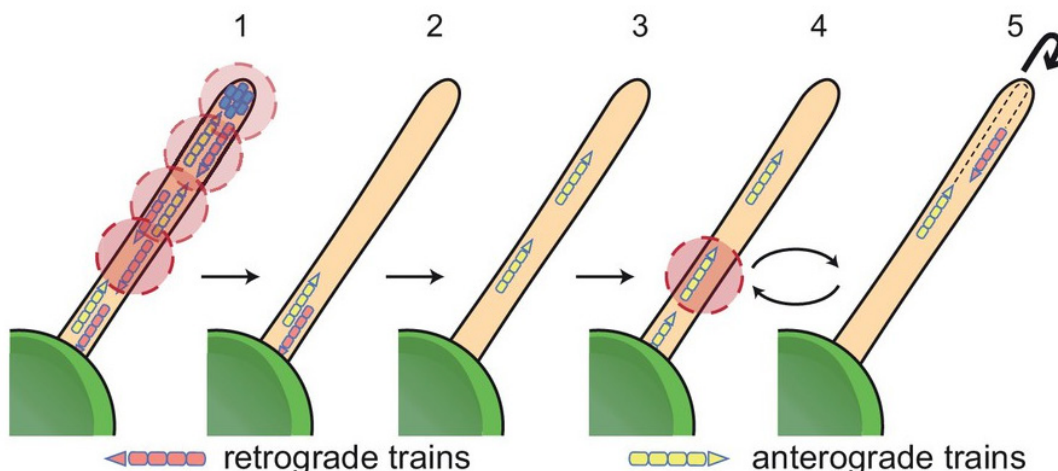
Figure 1.7. Schematic of the PhotoGate used to study the dynamics of single intraflagellar transport trains as they move to the flagellar tip, remodel, and return to the cell body.

To accomplish this experiment, we modify a standard TIRF microscopy set-up. The 488 nm excitation laser is split by a polarizing beam splitter cube. Part of the laser is sent to a piezo-driven steerable mirror that is conjugate to the back focal plane of the objective. The amount of laser power directed to this PhotoGate path is determined by the polarization of light before the beamsplitter cube, which can be adjusted using a half-wave plate. The rotation of the beam at the piezo mirror creates a translation of the focused beam in the image plane. This beam is steered with a computer mouse using custom LabVIEW software.

Figure 1.8. Image from "PhotoGate microscopy to track single molecules in crowded

11

environments," From Belyy et al., 2017.

The gate beam is very bright and its reflected illumination overpowers the signal from fluorescent proteins in the flagellum, even when filtered with the proper fluorescence emission filter. Moreover, there are concerns that constant exposure to a focused laser beam may cause unintended side effects for the cell being imaged. To minimize these concerns, the PhotoGate beam is flickered for fractions of a second during experiments. This allows us to bleach fluorescent proteins entering the flagella while still allowing unbleached proteins to be viewed during the time that the gate beam is off.

The gate beam needs to be flickered frequently enough to bleach all incoming anterograde trains. Therefore, its frequency is depended on IFT train speed and the size of the bleaching beam. The beam must be flickered often enough such that an IFT train cannot possibly pass through its diameter in the time in which the beam is off. We purposely slightly defocused the bleaching beam in the image plane to allow for a larger photobleaching spot (approximately 2-3 μm). Because anterograde IFT trains travel at approximately 2 μm/s, we were able to use this beam to bleach all incoming trains by flickering once per second.

For some experiments, it became necessary to use the PhotoGate to study two orthogonally fluorescently tagged proteins using the PhotoGate. To accomplish that, we used an image-splitting device and dichroic mirror to spectrally separate the images from GFP and mCherry fluorescent channels. Moreover, because of some spectral bleed-through, we used time-sharing imaging to alternate GFP and mCherry excitation. To photobleach both proteins simultaneously, we took advantage of the fact that both GFP and mCherry fluorophores can be bleached and excited by 488 nm light. Therefore, a single wavelength of PhotoGate beam was sufficient for performing the experiment on both proteins. However, it should theoretically be feasible to use the PhotoGate with two separate but co-aligned laser wavelengths.

Results

**Chapter 2: Dynamics of the IFT machinery at the flagellar tip**

IFT trains split apart and mix with each other at the flagellar tip

To monitor IFT movement, we tracked the dynamic behavior of IFT27, a core component of the IFT complex B, in a *pf18 IFT27-GFP* strain (Engel et al., 2009; Qin et al., 2007). This strain has paralyzed flagella *(pf)* that readily adhere to the glass surface, enabling us to monitor IFT under total internal reflection (TIR) illumination (Engel et al., 2009). Consistent with previous studies (Dentler, 2005; Engel et al., 2009; Iomini et al., 2001; Kozminski et al., 1993; Qin et al., 2007; Shih et al., 2013), IFT trains moved processively along the length of flagella, reversing direction at the flagellar tip and base (Figure 2.1a, Video 1). Pausing and reversals of anterograde trains before reaching the tip were very rare. The velocity of IFT27-GFP was 2.1 ± 0.4 µm s^{-1} in the anterograde direction and 3.0 ± 0.7 µm s^{-1} in the retrograde direction (Figure 2.2, mean ± s.d., N = 80 trains in each direction). Because a large number of GFP-labeled trains accumulated at the tip, the dwell and departure of individual trains at the tip could not be resolved by conventional TIR imaging (Figure 2.1a).

To monitor the turnaround behavior of individual IFT trains at the flagellar tip, we developed the one-dimensional PhotoGate assay (Belyy et al., 2017) to track single fluorescent complexes at the flagellar tip. In this assay, fluorescent trains located at distal parts of a flagellum were initially photobleached by moving a focused laser beam from the tip of the flagellum to near its base. We next opened the "gate" by turning off the focused beam until a single fluorescent train entered the flagellum. The gate beam was repeatedly turned on for 0.2 s at 1 Hz to photobleach any additional anterograde trains entering the flagellum (Figure 2.1b, Video 2). Under these conditions, less than 1% of anterograde IFT trains were able to pass the gate unbleached. This approach revealed the full range of movement of single fluorescent IFT trains within the flagellum. IFT movement can be divided into three stages: anterograde movement toward the tip, pausing at the tip, and returning to the base by retrograde transport.

We directly observed that a single anterograde train splits into multiple retrograde trains at the tip (Figure 2.1c-e, Figure 2.3a). On average, 2.4 retrograde trains were detected departing from the tip after the arrival of a single fluorescent anterograde train (Figure 2.1f, N = 97), consistent with higher frequencies of retrograde IFT trains than anterograde IFT trains (Dentler, 2005; Iomini et al., 2001; Qin et al., 2007). However, the number of retrograde trains per fluorescent anterograde train in PhotoGate assays (2.4, Figure 2.1c) was significantly higher (Welch's t-test, p = 10^{-20}) than the ratios of retrograde to anterograde train frequencies (1.15, Figure 2.1a) (Dentler, 2005; Iomini et al., 2001; Reck et al., 2016). These observations suggested that IFT complexes from different anterograde trains recombine with each other to form retrograde trains at the tip. To test this possibility, we closed the gate after two or three fluorescent anterograde trains entered the flagellum (Figure 2.1d,e, Videos 3 and 4) and measured the number and return frequency of retrograde trains departing from the tip. If individual trains split and return without mixing with each other, the number and frequency of fluorescent retrograde trains would be proportional to the number of fluorescent anterograde trains. In contrast, we observed 2.4, 3.6, and 4.2 returning trains on average for one, two, and three incoming trains, respectively (N = 97, 60, 42, Figure 2.1f). The return frequencies for one, two, and three incoming fluorescent trains were 0.57, 0.71, and 0.76 s^{-1}, respectively. Because the increase was sub-proportional with the number of anterograde trains, we concluded that the fluorescent complexes in the anterograde trains

disassemble and mix with a pool of "dark" complexes from the other photobleached trains at the tip before they reorganize into retrograde trains (Figure 2.1f). Monte Carlo simulations revealed that our conclusions are not markedly affected by the limited number of IFT27-GFPs per anterograde train (~6) or GFP photobleaching under TIR illumination (0.07 s^{-1}, Figure 2.1g, Figure 2.4, see Materials and Methods).
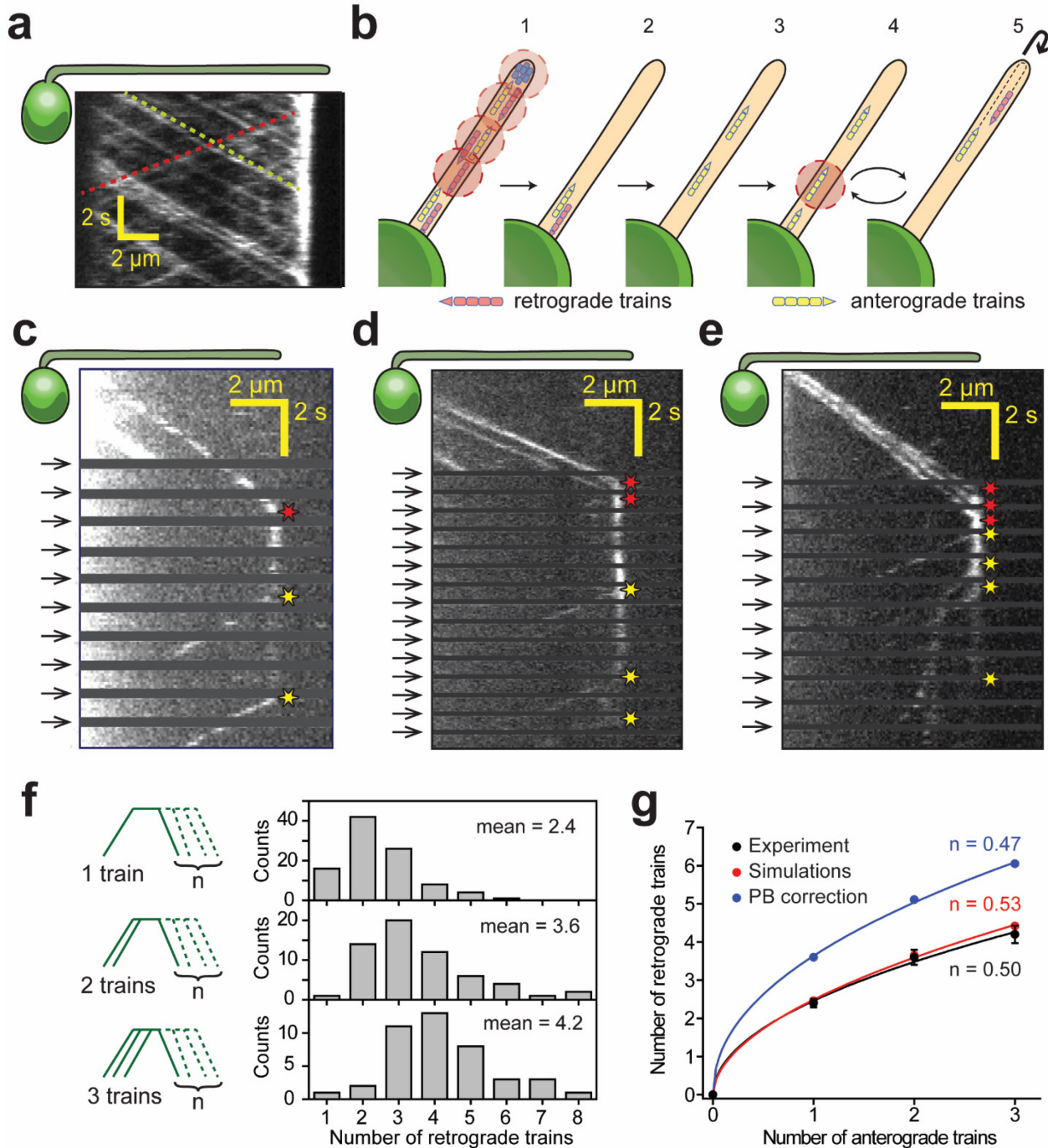
**Figure 2.1. IFT trains split apart and mix with each other at the flagellar tip.**
(**a**) Kymograph of a surface-immobilized *pf18 IFT27-GFP* strain shows that IFT trains move

bidirectionally along the flagellum, only reversing direction at the tip and the base. Multiple IFT trains accumulate at the flagellar tip. Representative anterograde and retrograde trajectories are shown with yellow and red dashed lines, respectively. (**b**) Schematic representation of the PhotoGate assay. 1) The distal half of the flagellum is prebleached by moving the powerful gate beam from the flagellar tip to near the base of the flagellum. 2-3) The gate beam is turned off to allow a single anterograde train to enter the flagellum without photobleaching. 4) The beam is then repeatedly turned on to photobleach the successive trains entering the flagellum and 5) turned off for 0.8 s to image the single fluorescent train within the flagellum. Photobleached trains are not shown. (**c-e**) Kymographs of one (c), two (d) and three (e) fluorescent anterograde trains entering the flagellum. Anterograde trains pause at the flagellar tip and split into multiple retrograde trains that move back to the base. Arrival of fluorescent anterograde trains and departure of retrograde trains at the tip are shown with red and yellow stars, respectively. Arrows represent repetitive bleaching events near the base of the flagellum. (**f**) (Left) The number of fluorescent retrograde trains was quantified as a function of one, two or three fluorescent anterograde trains entering the flagellum after photobleaching. (Right) The average number of retrograde trains increased sub-proportionally with the number of fluorescent anterograde trains entering the flagellum. N = 97, 60, 42 train events from top to bottom, in 160 cells, from 13 independent experiments. (**g**) The number of detectable retrograde trains versus the numbers of incoming anterograde trains in PhotoGate experiments and Monte Carlo simulations (PB: photobleaching). Solid lines represent the fit of data to the power law ($y = ax^n$). n is less than 1 under each condition. Error bars represent s.e.m. (N = 10,000 for simulations).
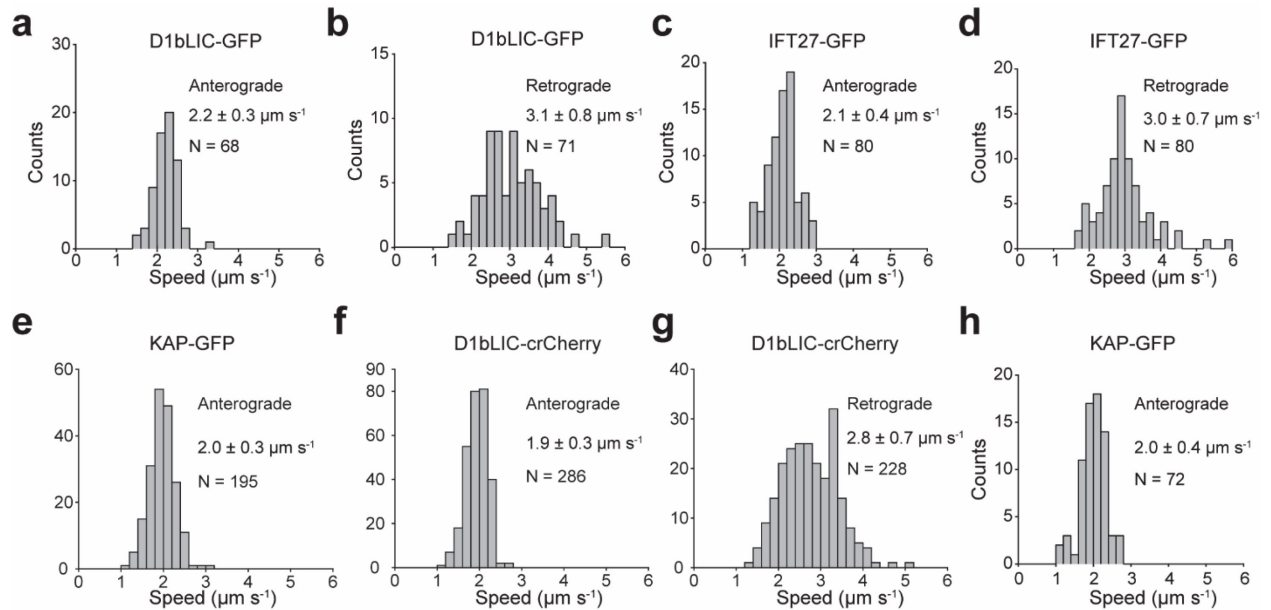
**Figure 2.2. Anterograde and retrograde velocities of epitope-tagged IFT27, KAP, and D1bLIC.**

(**a,b**) Anterograde (a) and retrograde (b) velocities of D1bLIC-GFP in *d1blic::D1bLIC-GFP* cells. (**c, d**) Anterograde (c) and retrograde (d) velocities of IFT27-GFP in *pf18 IFT-27-GFP* cells**.** (**e**) Anterograde velocities of KAP-GFP in *d1blic::D1bLIC-crCherry KAP-GFP* cells. (**f, g**) Anterograde (f) and retrograde (g) velocities of D1bLIC-crCherry in d*1blic::D1bLIC-crCherry KAP-GFP* cells. (**h**) Anterograde velocities of KAP-GFP in *fla3::KAP-GFP* cells. All velocities are reported as mean ± s.d. N represents the number of trains measured.
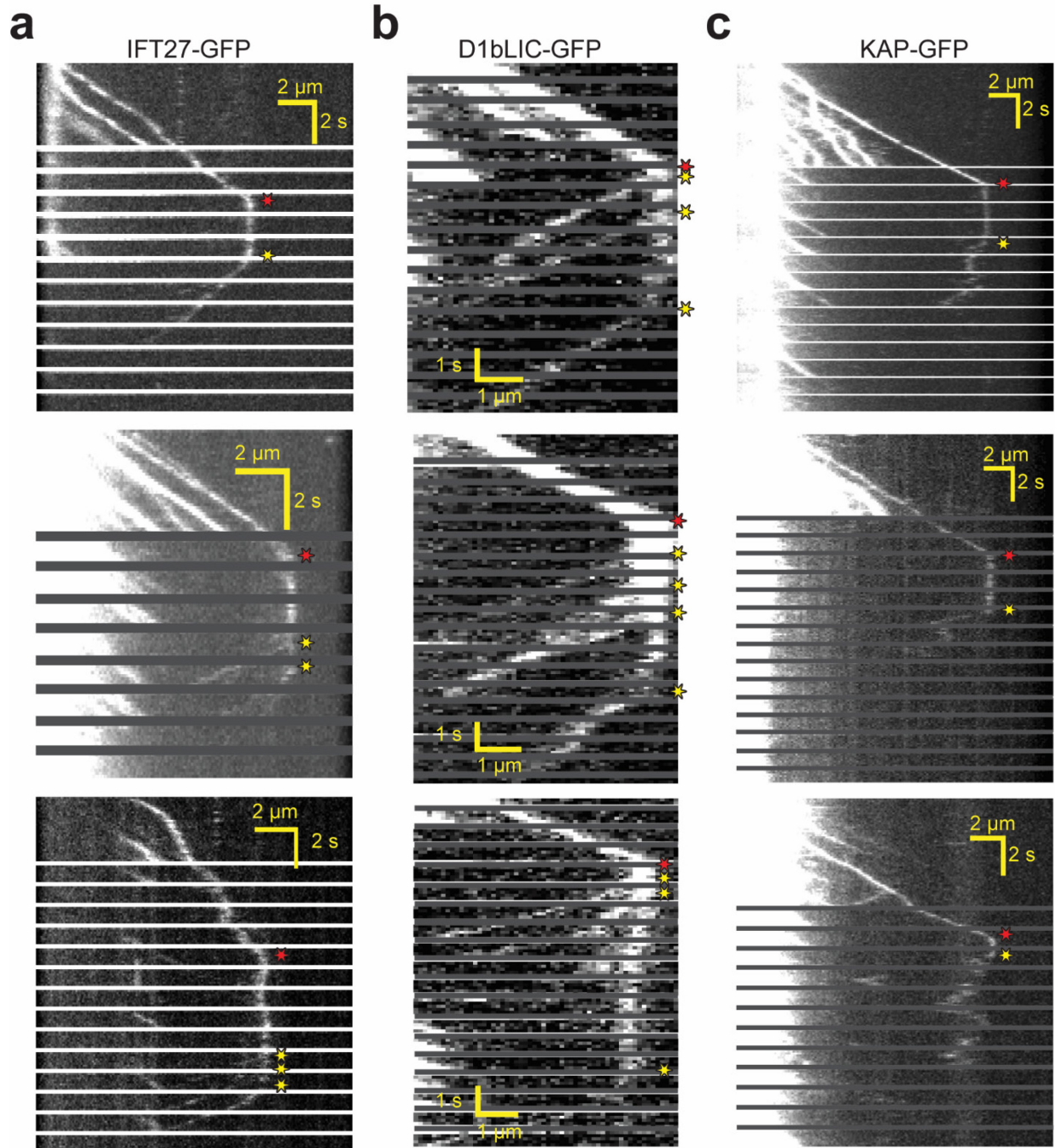
Figure 2.3. Additional examples for PhotoGate imaging of IFT27, D1bLIC, and KAP.

(**a**) IFT27 is moved to the tip on anterograde trains, remodels, and returns to the flagellar base on retrograde trains. (**b**) Dynein is moved to the tip on anterograde trains, remodels, and moves retrogradely to the cell body. (**c**) Kinesin moves anterograde trains to the flagellar tip, dissociates from the IFT trains at the tip, and diffuses within the flagellum. Red and yellow stars indicate arrival to and departure from the tip, respectively.
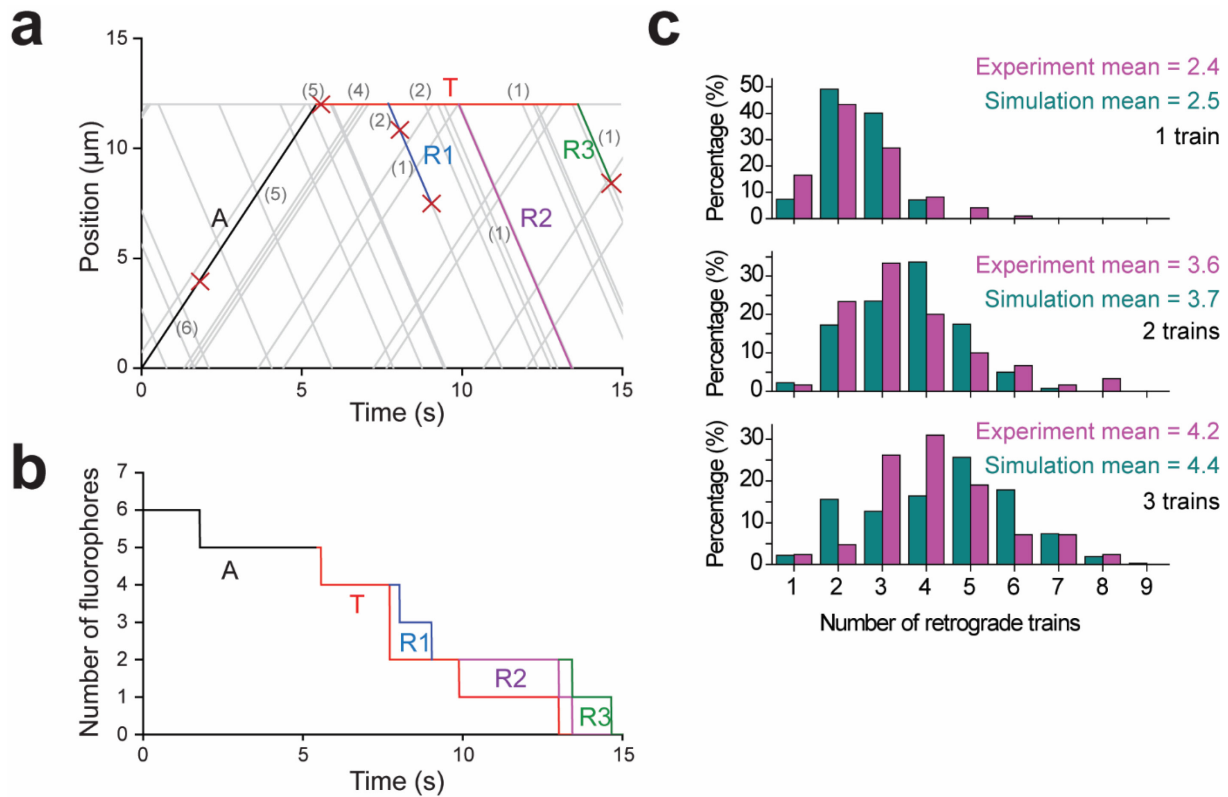
Figure 2.4. Monte Carlo simulations for the dynamics of IFT trains at the flagellar tip.

(a) A simulated kymograph with one anterograde IFT train (label A, black line) reaching the flagellar tip, joining the pool at the tip (label T, red line), and returning as three retrograde IFT trains (label R1-R3; blue, purple, and green lines). The anterograde train originally carries 6 bright fluorophores, and each fluorophore either bleaches or returns back to the flagellar base. The number of fluorophores is labeled in grey color within parentheses, and each bleaching event is indicated by a red cross. **(b)** The total number of fluorophores in the anterograde train (label A, black line), at the flagellar tip (label T, red line), and the retrograde trains (label R1-R3, blue line, purple line and green line) are shown as a function of time for the example kymograph shown in (a). Step-by-step reduction in GFP numbers in anterograde and retrograde trains is due to photobleaching of GFPs at 0.07 s^{-1} under TIR illumination. **(c)** The number of detectable retrograde trains in PhotoGate assays with one, two, and three fluorescent anterograde trains arriving at the tip in experiments (Figure 1f) and Monte Carlo simulations (N = 10,000 for simulations).

IFT tip turnaround is regulated by dynein activity and extracellular Ca^{2+}

To understand processing of IFT trains at the tip, we analyzed the time between the arrival of an anterograde train and the departure of fluorescent retrograde trains (referred to as tip resting time) at the tip (Figure 2.5a). When only a single fluorescent anterograde IFT27-GFP train was left unbleached near the base of the flagellum, the tip resting time of the 1st retrograde train was 3.1 ± 0.3 s (mean ± s.e.m., N = 97, Figure 2.5b), comparable to that of IFT cargos (Craft et al., 2015; Reck et al., 2016; Wren et al., 2013). Tip resting time was independent of flagellar length (Figure 2.6). If IFT tip turnaround was rate-limited by a single process, we would expect a single exponential distribution of tip resting times. However, the tip resting time histogram of 1st retrograde trains fit well to a Gamma distribution with a shape parameter of 3 and a rate constant of ~1 s^{-1}, indicating that tip turnaround of IFT trains occurs rapidly through a multistep process (Figure 2.5b). We also observed that the tip resting time of 1st, 2nd, 3rd, and 4th fluorescent retrograde trains increases linearly (Figure 2.5c). Because the average time between successive retrograde trains (Δt = 1.7 s) is the same, we concluded that the tip departure is a purely stochastic process. The linear fit to the tip resting times has a y-intercept of 1.3 s (Figure 2.5c), revealing that the departure of the 1st train takes longer than Δt. Therefore, the complexes dwell at the tip through another rate limiting process before they can depart from the tip.

When two or three fluorescent anterograde trains were allowed to pass through the gate, Δt became shorter (1.4 and 1.3 s, Welch's t-test, p = 0.03 and 0.02 for two and three trains, respectively; Figure 2.5c). This is because providing a higher number of fluorescent GFPs available at the tip increases the likelihood of retrograde trains to have at least one fluorescent GFP. Remarkably, the y-intercept remained constant when we allowed one to three more fluorescent anterograde trains to enter the flagellum (Figure 2.5c), suggesting that this duration corresponds to processing and breakdown of anterograde trains at the tip (referred to as tip remodeling time). The time between tip remodeling and departure of IFT trains is defined as the tip departure time (Figure 2.5a).

We also tested whether extracellular calcium and the dynein inhibitor ciliobrevin D (Firestone et al., 2012) affect the duration of IFT tip turnaround. Calcium regulates pausing of IFT trains along the flagellum (Collingridge et al., 2013; Shih et al., 2013), and disrupting calcium-dependent kinesin-II phosphorylation causes abnormal accumulations of IFT proteins at the ciliary tip (Liang et al., 2014). When extracellular calcium in media (0.34 mM) was chelated using 0.5 mM EGTA, the tip departure time increased to 2.8 s (Welch's t-test, p = 0.01), whereas tip remodeling time (1.4 s) remained unaltered (Figure 2.5d,e). Therefore, calcium has minimal effect on the breakdown of anterograde trains, but may have a regulatory role in the assembly or departure of retrograde trains. Addition of 0.1 mM ciliobrevin D to media results in 50% reduction in the frequency of retrograde and anterograde trains, and 50% and 28% reduction in retrograde and anterograde train velocities, respectively (Shih et al., 2013). In this case, the tip resting time of IFT27 increased over two-fold (Figure 2.5e, p <10^{-4}), suggesting that rapid turnover of IFT trains depends on dynein activity.
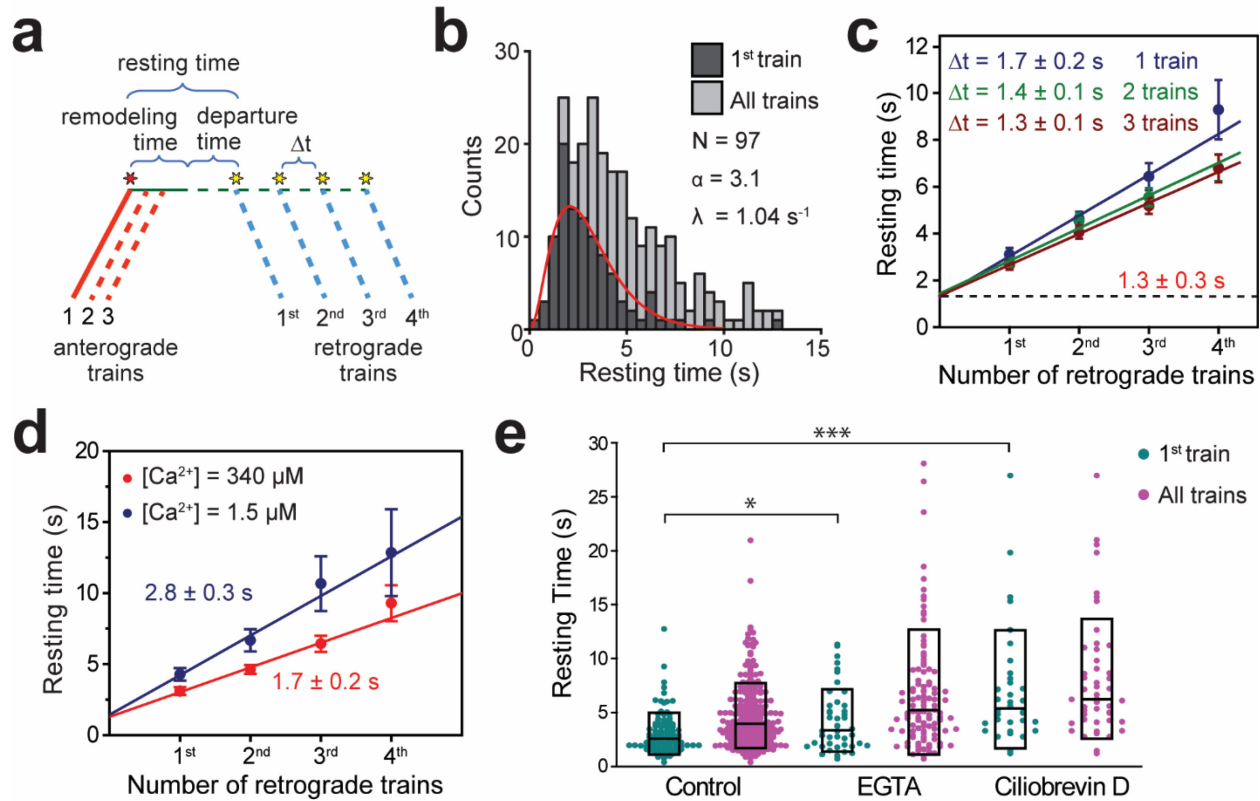
Figure 2.5. Tip turnaround of IFT trains is a multistep process regulated by dynein activity and extracellular Ca^{2+}.
(**a**) The schematic describes the definition of tip resting time, remodeling time, and departure time measured from the kymographs. Arrival of the first fluorescent anterograde train and the departure of retrograde trains are shown with red and yellow stars, respectively. Tip resting time and departure time are only shown for the first retrograde train. Tip remodeling time is assumed to be the same for each train. Δt represents the time between the departure of successive retrograde trains. (**b**) The resting time histogram of the first retrograde IFT27-GFP train (dark grey) and all of the trains (light grey) emanating from a single anterograde train. The histogram of the first retrograde trains was fitted to a Gamma function (red curve). α and λ are shape and rate parameters, respectively. (**c**) The linear fit to the average tip resting time reveals Δt between successive trains. The y-intercept (black dashed line) represents the tip remodeling time. Errors represent standard error of the linear fit. (**d**) Average tip resting times of the 1st, 2nd, 3rd and 4th retrograde IFT27-GFP trains coming out of an anterograde train for cells in TAP media (red, N = 97) and calcium-depleted media (blue, N = 44). Errors represent standard error of the linear fit. (**e**) IFT27-GFP tip resting times in 0.5 mM EGTA and 0.1 mM ciliobrevin D treated cells. The line within the boxplot represents the mean. The outer edges of the box represent standard deviation. N = 97, 44, 34, 34, 52 retrograde trains from left to right, in a total of 22 independent experiments (Welch's t-test, *p < 0.05, ***p < 0.001, as compared to no treatment for first retrograde trains).
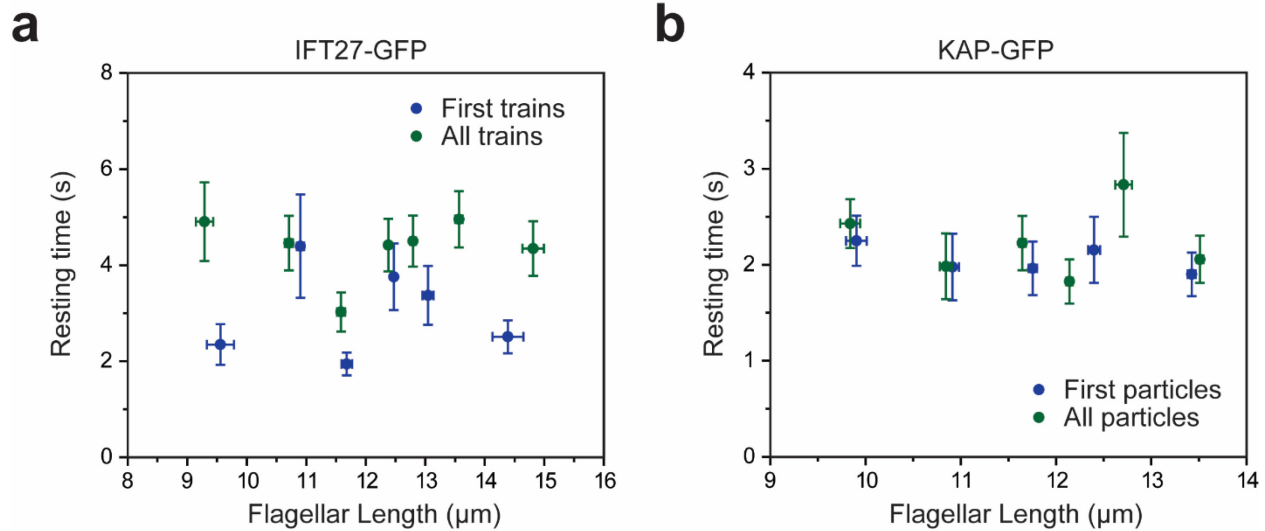
Figure 2.6. Tip resting time is independent of flagellar length.

(**a,b**) The average tip resting time of IFT27-GFP trains (a) and KAP-GFP particles (b) at different lengths of steady-state flagella. Error bars in both axes represent s.e.m. For IFT27-GFP, N = 60 (first train) and 136 (all trains). The bin size is 10 particles. For KAP-GFP, N = 95 (first particle) and 111 (all particles). The bin size is 20 particles.

## Kinesin-II dissociates from IFT trains at the tip

We next turned our attention to the movement of the IFT motors and their exchange at the flagellar tip. Dynein-1b was tagged with GFP at its light intermediate chain (D1bLIC), which assembles into the dynein-1b complex and rescues *d1blic* mutant phenotypes (Reck et al., 2016). In the *d1blic::D1bLIC-GFP* strain, D1bLIC moved continuously in the anterograde and retrograde directions at velocities similar to that of the IFT trains (Reck et al., 2016) (Figure 2.7a, Figure 2.2). Kinesin-II was tagged with GFP at its non-motor subunit KAP that localizes kinesin-II to the flagellar base (Mueller et al., 2005). In the *fla3::KAP-GFP* strain, KAP moved primarily in the anterograde direction to the flagellar tip at a similar speed to anterograde IFT27 (Figure 2.7b, Figure 2.2). Unlike D1bLIC, retrograde traces of KAP were not frequently observed (Engel et al., 2009; Wingfield et al., 2017), suggesting that kinesin-II dissociates from IFT trains at the tip (Engel et al., 2009, 2012).

PhotoGate assays revealed that D1bLIC-GFP has similar tip turnaround dynamics to IFT27-GFP (Figure 2.7c, figure 2.3b, Video 5). After arrival of a single anterograde D1bLIC-GFP train at the tip, we detected on average 2.5 retrograde D1bLIC trains. The average tip resting time until the departure of the first retrograde train was 1.8 ± 0.2 s (mean ± s.e.m., N = 60, Figure 2.7d), with additional ~1.1 ± 0.1 s between subsequent departure events (Figure 2.7e). PhotoGate imaging of KAP-GFP cells showed that single KAP-GFP trains moved anterogradely to the tip and rested at the tip for 2.2 ± 0.2 s (N = 95). Unlike D1bLIC, individual KAP-GFP particles moved away from the tip by rapid saltatory motion (Figure 2.7f,g, Figure 2.3c, Video 6). Mean square displacement (MSD) analysis showed that KAP undergoes one-dimensional diffusion at 1.68 ± 0.04 μm^2 s^{-1}

(mean ± s.e.m., N = 27 traces) within the flagellum after it departs from the tip (Figure 2.7h), consistent with the values measured for tubulin and EB1 that undergo diffusion within the ciliary space (Craft et al., 2015; Harris et al., 2016). The tip resting time of KAP remained nearly constant at different steady-state flagellar lengths (Figure 2.6) and was shorter than that of IFT27, indicating that departure of kinesin from the tip is independent of flagellar length and departure of retrograde trains (Figure 2.6).

Unlike IFT trains, the majority (89%, N = 95) of KAP-GFPs simultaneously departed from the tip in a single step (Figure 2.8). Because each anterograde train contains multiple (6) KAP-GFPs on average (Engel et al., 2009), this observation indicates that kinesin-II departs from the tip in the same oligomeric state as it arrives. 34% of kymographs clearly showed a single diffusing fluorescent spot after departure (Figure 2.7f), suggesting that KAPs are held together in a single complex. In 30% of kymographs, the KAP signal spread quickly along the length of a flagellum after departure, suggesting that kinesin-IIs can also diffuse alone (Figure 2.9, Video 7). The rest of the kymographs were ambiguous. Similar to IFT27, the tip resting time of KAP increased ~50% when the cells were treated with ciliobrevin D (p = 0.0016), but EGTA had no significant effect on tip resting time of KAP (Figure 2.8).

We next investigated whether KAP slides linearly along the microtubule track, similar to the non-processive, microtubule-depolymerizing kinesin MCAK (Helenius et al., 2006). In this case, KAP clusters are expected to move along the microtubule long axis, so the fluctuation in KAP position in the perpendicular axis would be similar to the error of single particle tracking. The KAP-GFP particles had lateral fluctuations of 19 ± 2 nm (mean ± s.d.) when moving in the anterograde direction. After departing from the tip, lateral fluctuations of diffusing spots increased to 65 ± 7 nm (Figure 2.7i,j), comparable to the radius of the axoneme. The intensity of fluorescent spots stayed relatively constant during anterograde transport and diffusion, suggesting that the measured lateral fluctuations are due to diffusive motion rather than decreased tracking precision. We concluded that after KAP detaches from the flagellar tip, it freely explores the space between the flagellar membrane and the axonemal surface rather than sliding along microtubules.
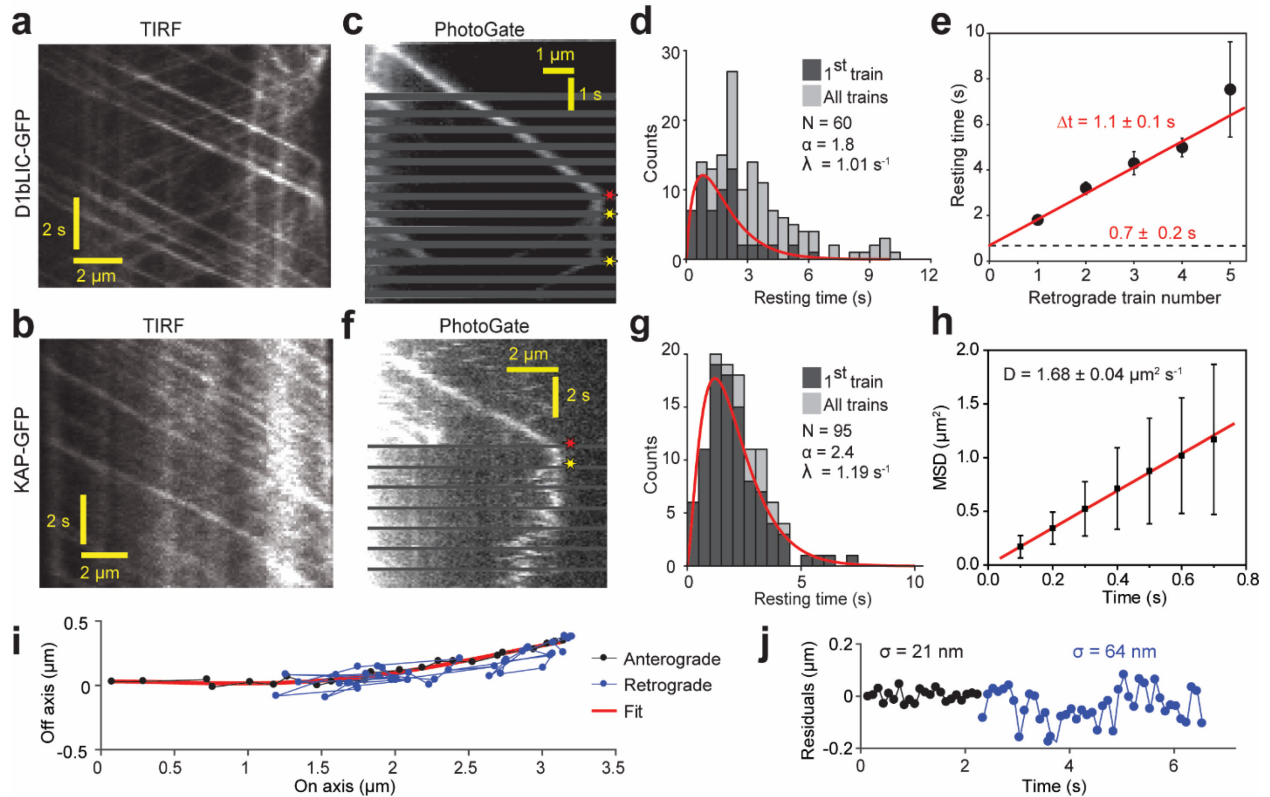
Figure 2.7. PhotoGate reveals the tip turnaround behavior of IFT motors.
(a) In a conventional TIR assay, anterograde and retrograde D1bLIC-GFP traces were clearly visible, but the tip behavior of individual trains could not be discerned. **(b)** In a conventional TIR assay, KAP-GFP was observed to move anterogradely, but the retrograde transport of KAP was rarely observed. **(c)** PhotoGate imaging of D1bLIC-GFP shows that D1bLIC trains move to the tip anterogradely, split into multiple trains, and return to the base retrogradely. Red and yellow stars indicate arrival to and departure of D1bLIC-GFP from the tip, respectively. **(d)** The tip resting time histogram of D1bLIC-GFP. Tip resting time of the first retrograde trains are fit to a Gamma distribution (red curve; 95% c.i. for α is 1.30-2.52 and for λ is 0.69-1.47 s^{-1}). N = 60 anterograde trains in 60 cells over 9 independent experiments. **(e)** Averaged tip resting time of the 1st, 2nd, 3rd, and 4th retrograde D1bLIC-GFP particles returning from the tip (mean ± s.e.m.). **(f)** Kymograph analysis of a KAP-GFP cell imaged by PhotoGate. KAP undergoes active transport in the anterograde direction, pauses at the flagellar tip, and diffuses back to the flagellar base. **(g)** The tip resting time histogram of KAP-GFP. The red curve represents a fit of first train resting times to a Gamma distribution. N = 95 anterograde trains in 47 cells over 4 independent experiments (95% c.i. for α is 1.87-3.19 and for λ is 0.88-1.60 s^{-1}). **(h)** MSD analysis of KAP-GFP movement after it leaves the flagellar tip. The average diffusion constant is 1.68 ± 0.04 μm^2 s^{-1} (N = 27, mean ± s.e.m.). **(i)** High-resolution tracking of a KAP-GFP particle reveals the two-dimensional trajectory during anterograde (black) and diffusion (blue). The red curve is the polynomial fit to the trace. **(j)** The residual plot to the trace in (i) reveals lateral fluctuations during anterograde transport (black) and diffusive (blue) movement.

23
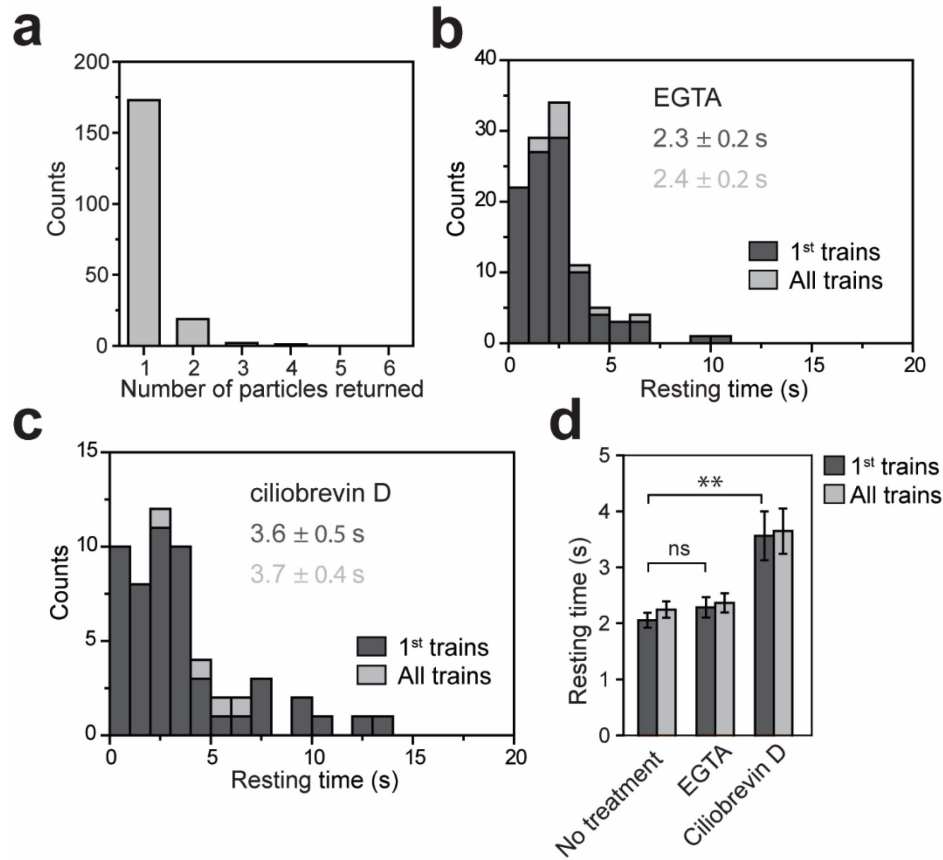
Figure 2.8. Tip resting time of KAP-GFP under various drug treatments. (a) The number of fluorescent KAP particles emanating from a single fluorescent anterograde KAP particle at the tip. N = 195 trains in 106 cells over 9 independent experiments. All KAP clusters displayed diffusive movement after leaving the tip. (**b**) The tip resting time histogram of KAP-GFP with EGTA treatment. N = 100 trains in 59 cells over 5 independent experiments. (**c**) Tip resting time histogram of KAP-GFP with ciliobrevin D treatment. N = 52 trains in 37 cells over 4 independent experiments. (**d**) The average tip resting time for KAP-GFP under EGTA and ciliobrevin D treatments (mean ± s.e.m.; **p < 0.01 as compared to no treatment; ns is non-significant).
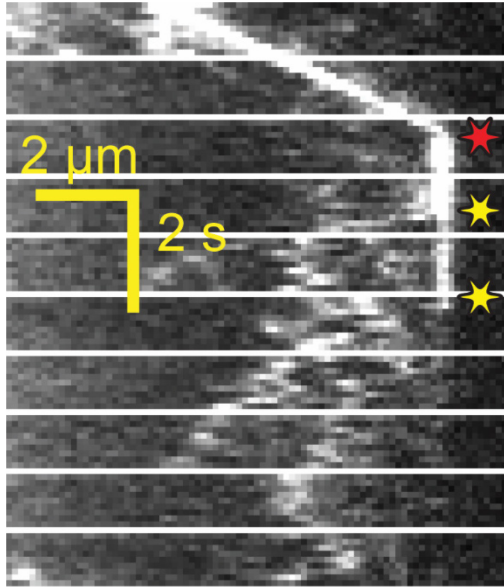
Figure 2.9. Example kymograph of KAP particle breaking apart after tip departure.

Kinesin moves anterograde trains to the flagellar tip, dissociates from the IFT trains at the tip, and diffuses within the flagellum. In this example, the KAP particle breaks apart into smaller particles while diffusing. Red and yellow stars indicate arrival to and departure from the tip, respectively.

Chapter 3: The recycling of molecular motors during IFT

Kinesin-II carries dynein-1b as an inactive passenger during anterograde IFT

To investigate how kinesin-II and dynein-1b motors interact with anterograde and retrograde trains and how they are recycled back to the basal body, we transformed a *d1blic* mutant with both *D1bLIC-crCherry* and *KAP-GFP* constructs and simultaneously tracked the movement of KAP and D1bLIC subunits in the rescued cells (Figure 3.2, Video 8). The *D1bLIC-crCherry* transgene rescued the flagellar assembly defects in the *d1blic* mutant, increasing the flagellar length to 12.2 ± 1.6 μm (mean ± s.d., N = 100 flagella). Both tagged motors were expressed at near wild-type levels (Figure 3.2). The velocities of anterograde and retrograde D1bLIC-crCherry trains were similar to those observed with IFT27-GFP (Figure 3.1a, Figure 2.2). We observed strong co-localization of D1bLIC-crCherry and KAP-GFP on anterograde trajectories (Figure 3.1a), demonstrating that dynein-1b is carried to the flagellar tip by kinesin-II. Only D1bLIC-crCherry trains showed robust retrograde transport, while retrograde traces of KAP-GFP were rarely observed, consistent with dissociation of kinesin-II from IFT trains at the tip.

To determine which motor first departs from the tip after the arrival of an anterograde train, we performed two-color Photogate experiments to simultaneously track KAP-GFP and D1bLIC-crCherry from individual anterograde trains (Figure 3.1b). Out of 21 cells, KAP began diffusive motion before the retrograde movement of D1bLIC in 10 cells (Figure 3.1b), D1bLIC left the tip before KAP in 8 cells (Figure 3.3), and both appeared to exit the tip simultaneously (within 0.24 s) in 3 cells. These results suggest that kinesin-II and dynein-1b exit the flagellar tip independently from each other.
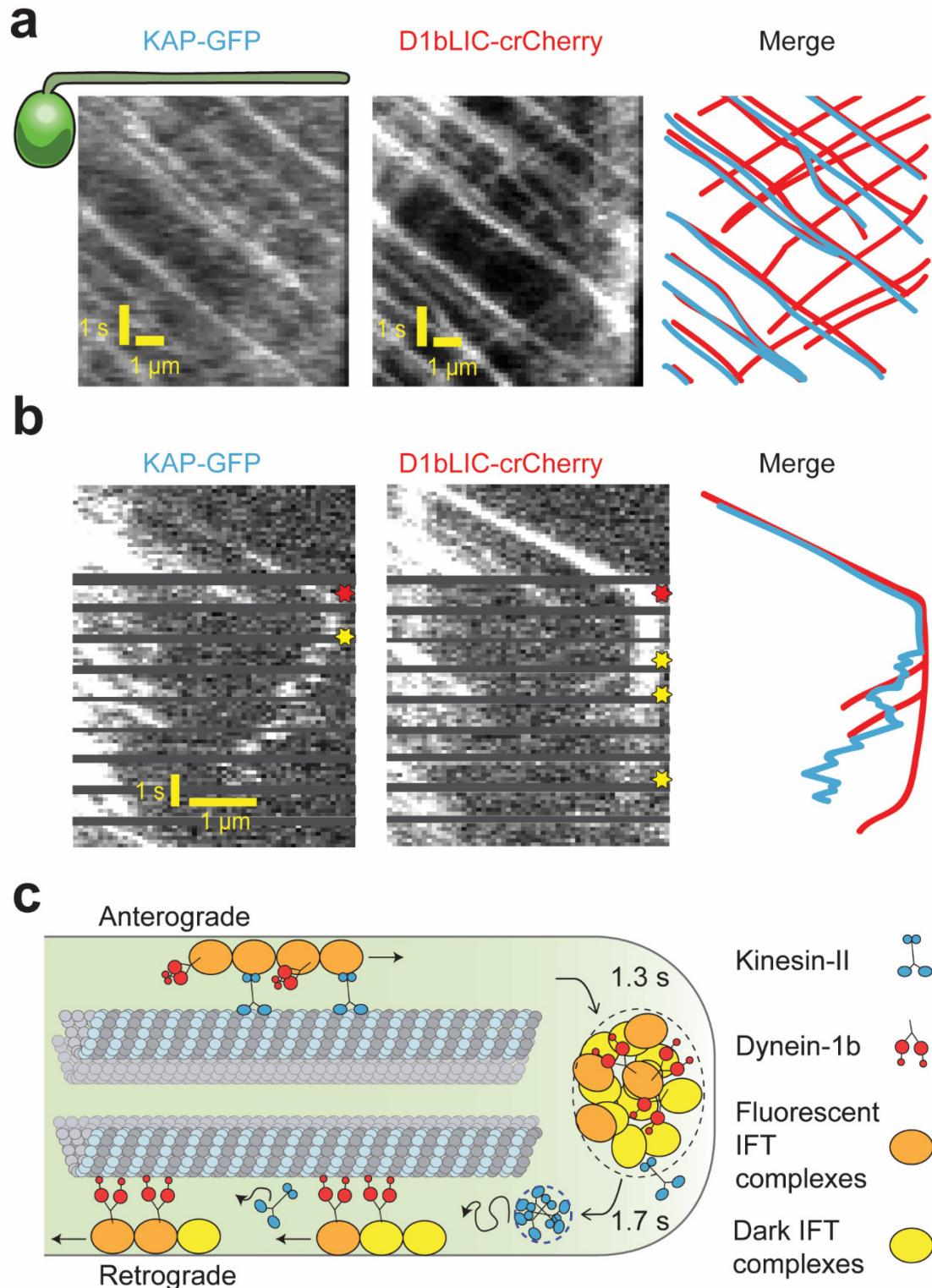
Figure 3.1. Transport roles of kinesin-II and dynein-1b.
(a) Representative kymographs of KAP-GFP and D1bLIC-crCherry in a *d1blic::D1bLIC-crCherry KAP-GFP* flagellum. KAP-GFP and D1bLIC-crCherry co-localize on the IFT trains in the anterograde direction. Retrograde tracks are seen in the D1bLIC-crCherry channel, but are rarely visible in the KAP-GFP channel. (**b**) Example two-color PhotoGate trace of KAP-GFP

27

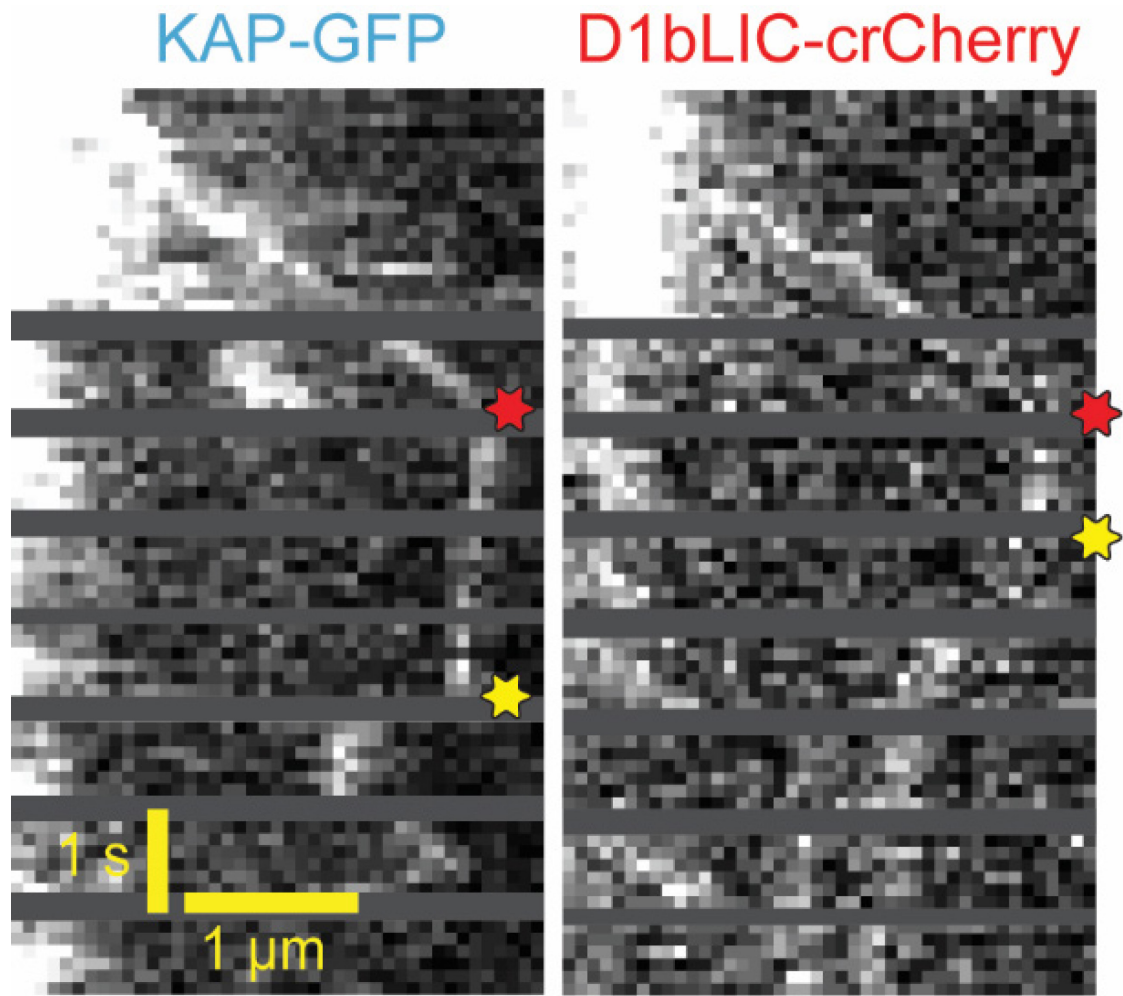(left) and D1bLIC-crCherry (middle) in single flagella. KAP-GFP and D1bLIC-crCherry arrive at the tip on the same train. In this example, KAP diffuses away from the tip before the departure of D1bLIC trains (right). Red and yellow stars indicate arrival to and departure from the flagellar tip, respectively. (**c**) A model for the turnover of IFT trains and motors at the flagellar tip. Kinesin-II motors transport individual anterograde IFT trains to the flagellar tip. Dynein-1b is carried with anterograde trains as an inactive passenger. At the tip, IFT complexes detach from microtubules, disassemble, and mix with the tip protein pool to assemble new trains. These trains are transported retrogradely by dynein-1b. Kinesin-II detaches from IFT trains at the flagellar tip and diffuses back to the base by diffusion either as a cluster (blue dashed circle) or individually.
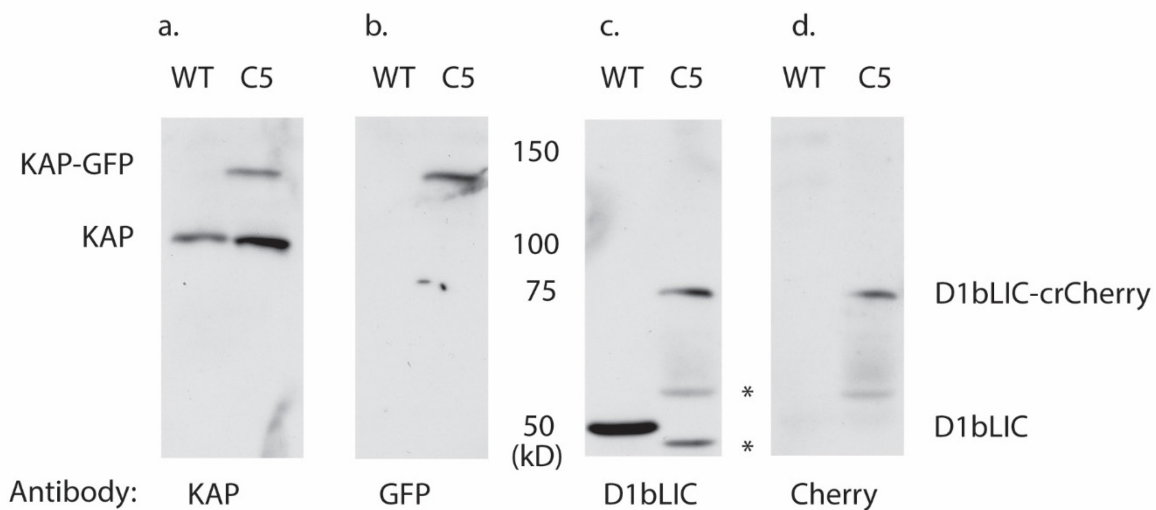
Figure 3.2. Expression of KAP-GFP and D1bLIC-crCherry in isolated flagella from a double-tagged strain.

Isolated flagella from wild-type cells (WT) and a *d1blic::D1bLIC-crCherry KAP-GFP* strain (C5) were analyzed on Western blots probed with antibodies against (**a**) KAP, (**b**) GFP, (**c**) D1bLIC, and (**d**) Cherry. The endogenous KAP subunit migrates at ~95 kD in both strains (a), and the KAP-GFP subunit migrates at ~122 kD (a, b). The D1bLIC subunit migrates at ~49 kD in WT (c) and the D1bLIC-crCherry migrates at ~75 kD in the C5 rescued strain (c, d). The lower molecular weight bands in the C5 rescued strain represent proteolytic fragments of the D1bLIC-crCherry polypeptide (black asterisks). These bands are variable in preparations of isolated flagella.

Figure 3.3. Example two-color PhotoGate trace of KAP-GFP (left) and D1bLIC-crCherry (right) in single flagella. KAP-GFP and D1bLIC-crCherry arrive at the tip on the same train. In this example, D1bLIC leaves the tip before KAP. Red and yellow stars indicate arrival to and departure from the flagellar tip, respectively.

**Kinesin-II returns from the ciliary tip to the cell body by diffusion**

Dissociation of KAP from IFT trains at the tip is consistent with the recycling of kinesin-II to the cell body in the absence of active retrograde IFT (Engel et al., 2012; Pedersen et al., 2006; Reck et al., 2016). However, it remained unclear how kinesin-II achieves this long-range movement without active transport. To test whether diffusion from the tip effectively recycles KAP to the cell body, we performed fluorescence recovery after photobleaching (FRAP) assays in the middle sections of full-length flagella of *fla3*::KAP-GFP cells (~12 µm, Figure 3.4a, Video 9). Directional movements of KAP-GFP labeled trains into the photobleached area were seen from the anterograde direction, whereas recovery of GFP fluorescence from the retrograde direction was primarily due to diffusion of KAP-GFP from the tip. These results suggest that the high levels of background observed in KAP-GFP flagella were caused by kinesin-II motors dissociated from IFT trains at the tip. The diffusion constant calculated from the fluorescence recovery (1.8 ± 0.1 µm^2 s^{-1}, Figure 3.4b) was similar to the result of the MSD analysis (Figure 2.7h). The fluorescent background in KAP-GFP flagella increased towards the tip, suggesting a net efflux of diffusing KAP-GFP towards the cell body (Figure 3.4c,d). During flagellar regrowth, the KAP-GFP gradient was maintained for all flagellar lengths (Figure 3.5a, see Materials and Methods). The influx of KAP-GFP fluorescence to the flagellum through anterograde IFT was statistically indistinguishable from the efflux of KAP-GFP to the base through one-dimensional diffusion in flagella (Welch's t-test, p = 0.80, N = 57, Figure 3.6, see Materials and Methods). These results strongly indicate that KAP-GFP returns to the cell body by diffusing from the flagellar tip.

We ran Monte Carlo simulations to estimate the accumulation of KAP in a flagellum at a steady-state using the measured values of IFT train loading (Engel et al., 2009), diffusion coefficient, flagellar length, and IFT train frequency. The model assumes that KAP is released from anterograde IFT trains at the tip, diffuses within a flagellum, and is taken up by the basal body. Under these conditions, simulations confirmed the build-up of a linear concentration gradient of KAP in the flagellum (Figure 3.5b). In fully-grown flagella, the return of KAP to the flagellar base takes 42 s on average, an order of magnitude longer than the travel of retrograde trains (4 s) to the base. This delay leads to a ~4-fold higher amount of KAP inside the flagellum compared to a case in which KAP returns to the base with retrograde trains (Figure 3.5c). Unlike KAP, IFT27-GFP cells have a low fluorescence background without an obvious concentration gradient along the length of the flagellum (Figure 3.4d) due to active transport of the IFT trains in both directions.
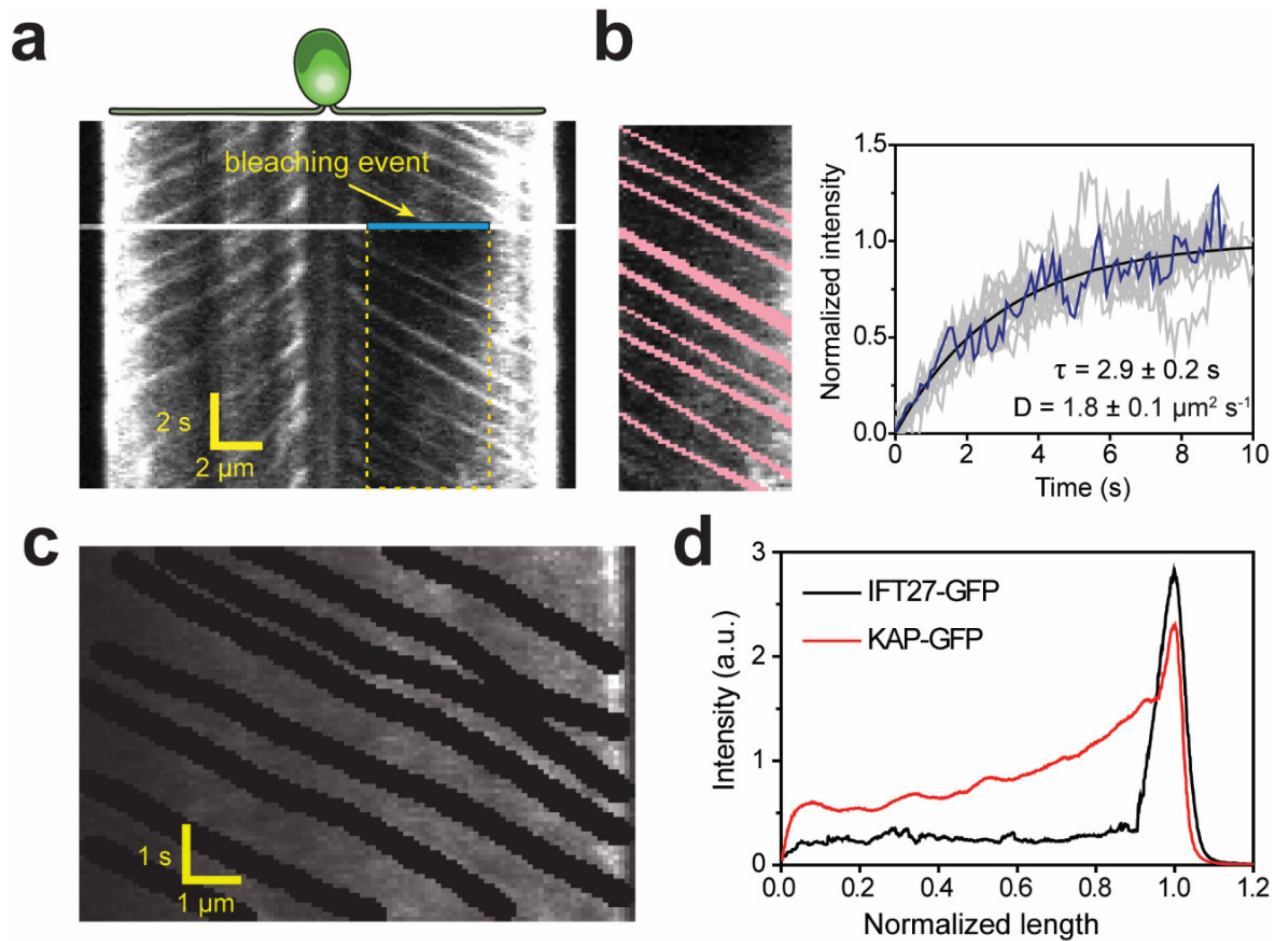
Figure 3.4. Diffusion of KAP from the flagellar tip leads to a concentration gradient along the flagellum.
(a) Kymograph of KAP-GFP movement before and after photobleaching the middle section of the flagellum (blue area). While fluorescence recovery from the base is through anterograde movement, the recovery from the tip region is due to diffusion. **(b)** (Left) The GFP signal of anterograde traces (red) was manually subtracted from the rectangular area shown in (a). (Right) The intensity in the photobleached area shows recovery as a function of time (blue line). The average recovery signal of 13 cells (grey lines) was fitted to a one-dimensional diffusion equation (black curve, ± 95% c.i.). **(c)** In conventional TIR imaging, anterograde trajectories of KAP-GFP were manually subtracted from the kymograph. **(d)** The average GFP signal along the length of a flagellum in KAP-GFP and IFT27-GFP cells after the removal of anterograde and retrograde transport traces from the kymographs. Flagellar base and tip positions were normalized to 0 and 1, respectively. N = 11 for both KAP-GFP and IFT27-GFP.
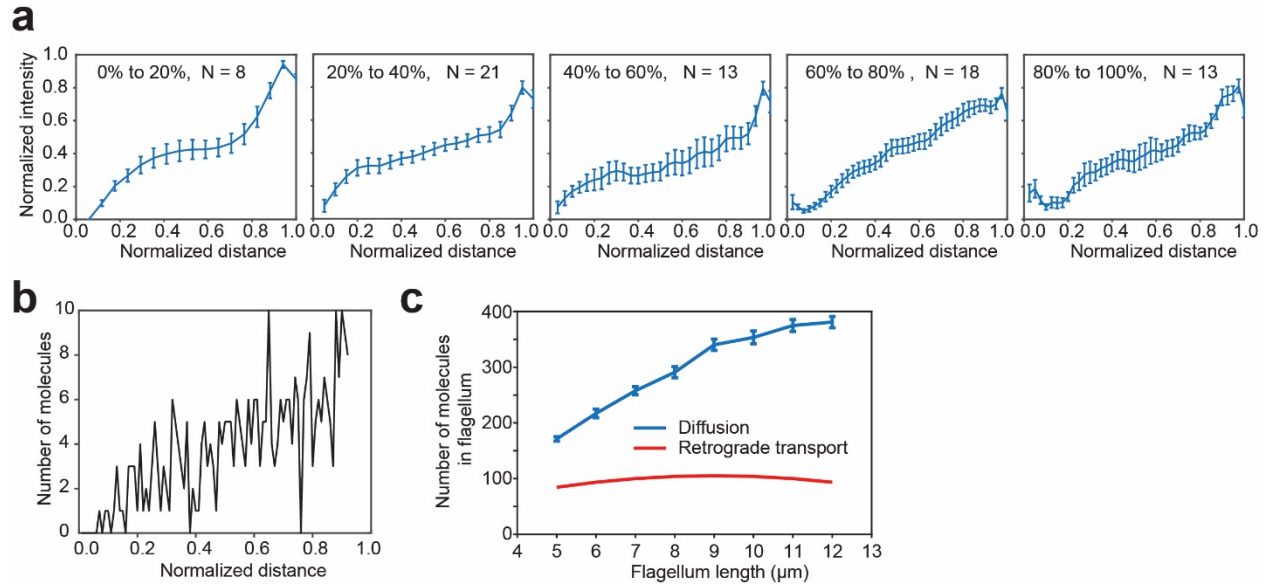
Figure 3.5. A gradient of KAP-GFP fluorescence along the length of the flagellum exists across all flagellar lengths.

(a) The gradient of KAP-GFP fluorescence is approximately linear over the length of the flagellum for flagella of different lengths. Cells undergoing flagellar regrowth were imaged and split into groups by their flagellar length, as a percentage of full-length flagella. IFT trains were manually removed from kymographs and remaining pixels were time-averaged to calculate the concentration gradient of the KAP-GFP. Error bars represent s.e.m. N = 57 kymographs over 5 independent experiments. **(b)** Monte Carlo simulations reveal the flagellar distribution of KAP-GFP diffusing from a source at the tip (right) to a sink at the base (left). **(c)** Simulations show that return of KAP to the cell body by diffusion leads to a greater accumulation of KAP in the flagellum, in comparison to a hypothetical case where KAP returns to the cell body via retrograde transport. This analysis accounts for both anterogradely moving and diffusing KAP molecules.
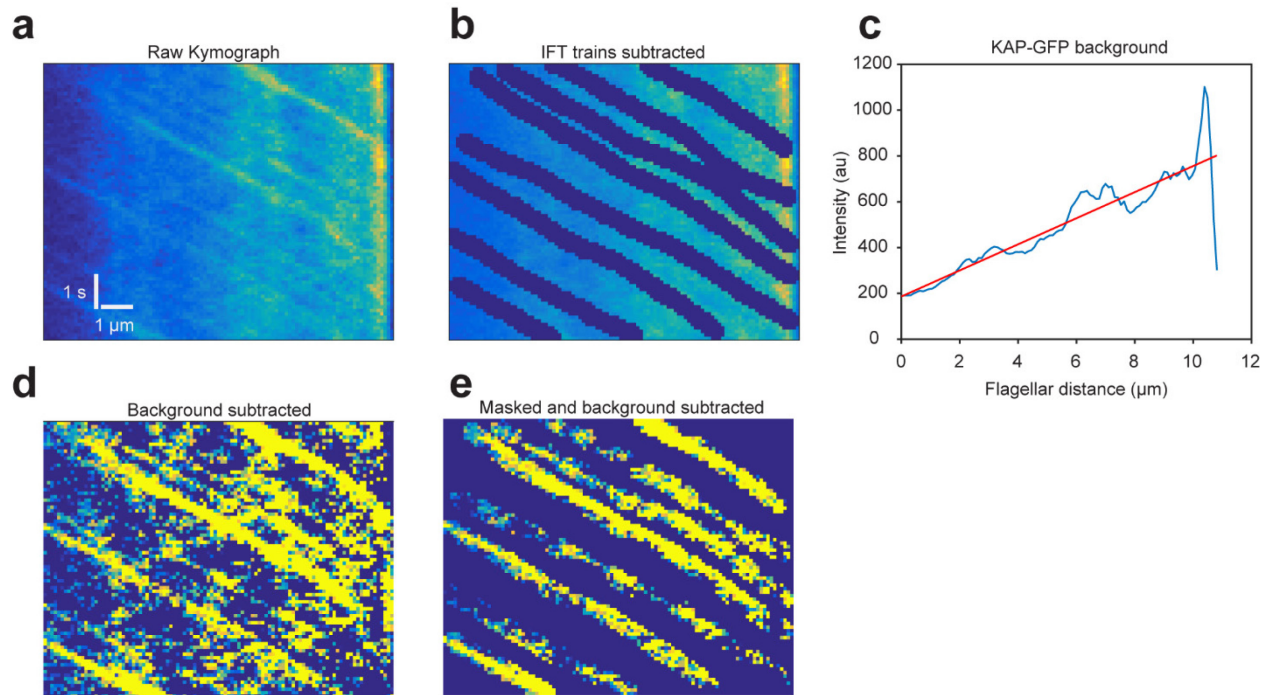
Figure 3.6. The influx and efflux of KAP-GFP fluorescence in fully grown flagella are equal.

(a) An example kymograph of a *fla3::KAP-GFP* flagellum imaged with TIR. The flagellar tip is on the right. **(b)** To calculate the intensity of the fluorescence background, anterograde trajectories of KAP were manually subtracted from the kymograph. **(c)** Intensities were time-averaged to calculate KAP-GFP background. Efflux was calculated from Fick's law using the slope of the intensity profile along the flagellar length and the measured diffusion constant (1.7 $\mu m^2 s^{-1}$). **(d)** Background was subtracted from original kymograph to get anterograde train intensities. **(e)** The kymograph was masked for anterograde trains to calculate the average fluorescent counts per train. Influx was calculated by multiplying counts per train with the measured train frequency (1.3 s^{-1}). KAP-GFP influx into the flagellum (1,130 ± 70 counts s^{-1}) was similar to the efflux of KAP from the flagellum (1,170 ± 160 counts s^{-1}). N = 57 kymographs over 5 independent experiments (mean ± s.e.m.).

Chapter 4: The role of IFT in flagellar length control

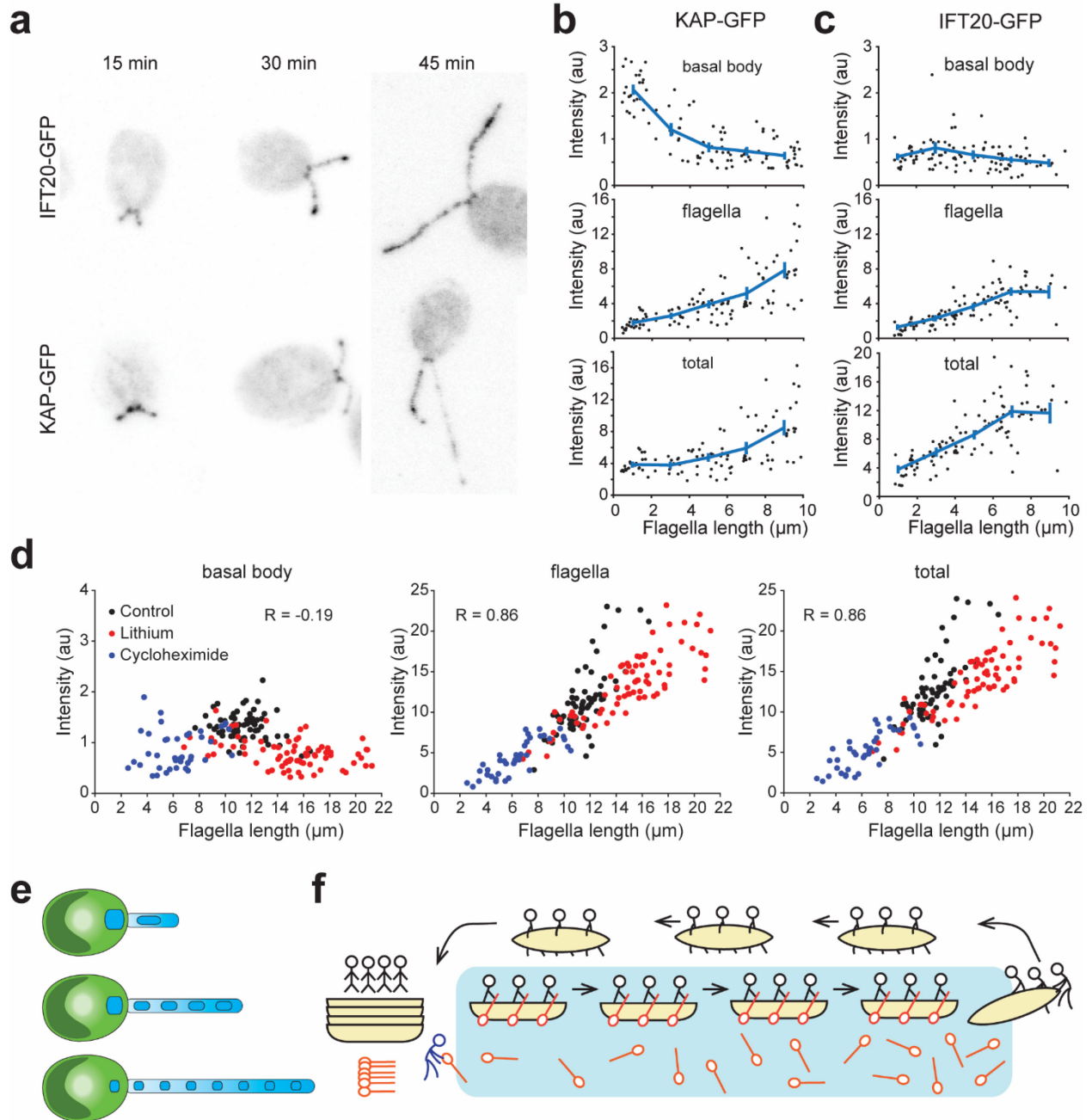### Kinesin-II is depleted from the basal body during flagellar regrowth

KAP-GFP loading on IFT particles has been shown to decrease with increasing flagellar length (Engel et al., 2009), but the underlying mechanism remained unclear. Because a larger amount of KAP builds up in the flagellum as the flagella elongate (Figure 3.5), loading of KAP onto the subsequent IFT trains may be reduced by depletion of KAP at the flagellar base. To test this model, we deflagellated *fla3::*KAP-GFP cells and measured the GFP fluorescence at the basal body and in the flagellum during flagellar regrowth using confocal microscopy (Figure 4.1a). We estimated that the total amount of KAP localized to the base and flagellum increased by two-fold with flagellar length, indicating the upregulation of IFT components during flagellar growth. The fluorescence intensity at the flagellar base was highest for short flagella (1-4 μm) and decreased ~4-fold as cells grew full-length flagella (~10 μm, Figure 4.1b), significantly larger than ~1.6-fold reduction reported previously (Ludington et al., 2015). We also observed that the KAP fluorescence in the flagellum was low in short flagella and increased ~10-fold as the flagellar length reached the steady-state (Figure 4.1b).

Changes in the amount of IFT complexes were markedly different from that of KAP during flagellar regrowth (Figure 4.1a). Unlike KAP-GFP, basal body fluorescence of IFT20-GFP remained nearly constant across all flagellar lengths in IFT20::IFT20-GFP cells (Figure 4.1c), presumably because they are rapidly returned to the base through active transport. We also observed an increase of the GFP signal in the flagellum with elongation (Figure 4.1c), in contrast to the previous observation that the total amount of IFT components remains constant during flagellar regeneration (Marshall and Rosenbaum, 2001). This discrepancy may be related to differences in methods for quantifying IFT components in flagella.

We next determined the localization of KAP-GFP to the basal body and flagellum in cells that grow abnormally long and short flagella. *Chlamydomonas* grows ~1.5X longer flagella in the presence of Li^+ (Nakamura et al., 1987) by recruiting flagellar proteins from the cell body pool into the flagella (Nakamura et al., 1987) rather than requiring new protein synthesis (Wilson and Lefebvre, 2004). Consistent with previous observations, the KAP-GFP strain grew longer flagella in 50 mM Li^+. After reaching the steady state length, we calculated the total KAP fluorescence at the basal body and the flagellum (Figure 4.1d, Figure 4.2). In agreement with our model, we observed that KAP gets depleted at the basal body at equilibrium. The KAP fluorescence localized to a flagellum correlated strongly with flagellar length (Pearson's R = 0.86), similar to untreated cells. The total KAP fluorescence in the flagellum was 50% higher than untreated cells.

In the absence of new protein synthesis, *Chlamydomonas* can grow half-length flagella after deflagellation, suggesting that the cytoplasmic pool of flagellar proteins is at least one half of that localized to the flagellar compartment (Rosenbaum et al., 1969). We deflagellated KAP-GFP cells with pH shock and regrew their flagella in the presence of the protein synthesis inhibitor cycloheximide. In agreement with untreated and Li^+ treated cells, we observed that the KAP fluorescence at the flagellum correlates strongly with the flagellar length (Pearson's R = 0.86), whereas the KAP intensity was depleted at the basal body (Figure 4.1d, Figure 3.2). Total KAP fluorescence was one half of untreated cells, consistent with the fact that a large amount of KAP is lost during deflagellation. Therefore, over a wide range of flagellar lengths (2 – 22 μm), KAP

gets depleted at the basal body when the flagella reach their equilibrium length.

Figure 4.1. Kinesin-II accumulates in flagella and is depleted at the basal body during flagellar growth.
(a) Representative confocal images show the distribution of IFT20-GFP and KAP-GFP fluorescence at the basal body region and in the flagella during flagellar regrowth. **(b,c)** Integrated KAP-GFP (b) and IFT20-GFP (c) fluorescence at the basal body (top), in the

flagellum (middle), and in both regions (bottom) at different flagellar lengths. Each black dot represents a single flagellum and the blue line is the running average (±s.e.m.). For KAP-GFP, N = 104 flagella from 70 cells over 2 independent experiments. For IFT20-GFP, N = 103 flagella from 56 cells over 2 independent experiments. **(d)** Integrated KAP-GFP fluorescence at the basal body (left), in the flagellum (middle), and in both regions (right) in control cells was compared to cells treated with 50 mM Li^{+}, and cells that regrow their flagella after cycloheximide treatment. R represents Pearson's correlation coefficient. Each dot represents a single flagellum. For control cells, N = 66 flagella from 33 cells. For lithium-treated cells, N = 74 flagella from 37 cells. For cycloheximide-treated cells, N = 40 flagella from 20 cells. **(e)** A model for flagellar length control. When the flagellum is short, IFT trains contain more kinesin-II from the large basal body pool. As flagella elongate, the number of kinesin-II per IFT train decreases because a significant fraction of the kinesin-II unloads at the tip and undergoes diffusion in the flagellar lumen, depleting the kinesin-II pool at the flagellar base. **(f)** An analogy for kinesin-II loading on IFT trains. Passengers (dynein-1b) travel from the left shore (basal body) to the right shore (flagellar tip) on a boat (IFT trains) with oars (kinesin-II). At the right shore, the passengers get out and walk the boats back to the dock. Oars are left on the water and can only be collected when they randomly float back to the left shore. If the distance between the shores is large, oars build up on the water and are not readily available for new boats at the left shore.
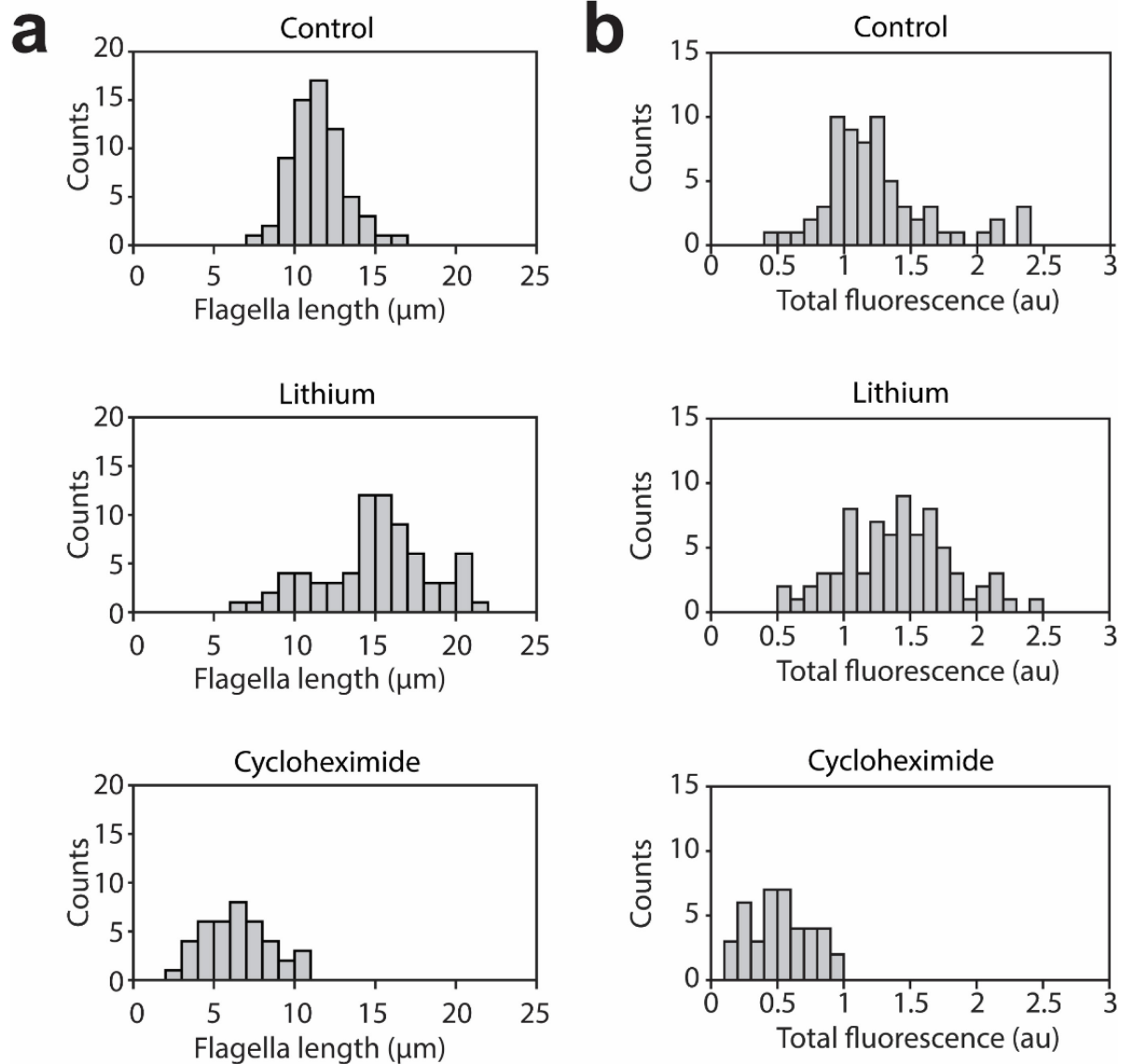
Figure 4.2. Length and total fluorescence distributions of lithium and cycloheximide-treated cells.

(a) Flagella length distributions for *fla3::KAP-GFP* cells cultured in TAP media, cells treated with 50 mM LiCl, and cells subjected to pH shock and allowed to regrow flagella in the presence of 1.5 ug/ml cycloheximide. For control cells, N = 66 flagella from 33 cells. For lithium-treated cells, N = 74 flagella from 37 cells. For cycloheximide-treated cells, N = 40 flagella from 20 cells. **(b)** Histograms show the total fluorescent signal of KAP-GFP localized to the basal body and the flagellum of single cells.

Discussion

Remodeling of IFT complexes and motors at the flagellar tip in *Chlamydomonas*

Using PhotoGate, we have visualized the turnaround behavior of individual components of the IFT machinery at the flagellar tip. We present evidence that when IFT trains arrive at the tip, the complexes split apart and mix with complexes from other trains at the flagellar tip before initiating retrograde transport (Figure 4c). This dynamic disassembly and reassembly process may lead to differences in size, shape, and structure of anterograde and retrograde trains, as previously suggested by transmission electron microscopy (Dentler, 2005; Stepanek and Pigino, 2016). Remarkably, remodeling of IFT trains is completed within 1.3 s, with a 1.7 s average waiting time between the departures of successive trains, consistent with previously measured values for IFT complex subunits, dynein-1b, and other axonemal cargoes (Craft et al., 2015; Qin et al., 2007; Reck et al., 2016; Wren et al., 2013). Kinetic analysis of the tip resting time revealed that disassembly of anterograde trains and reassembly of the retrograde trains is a multistep process regulated by extracellular calcium and the concentration of active dynein motors.

Simultaneous tracking of the anterograde motor kinesin-II (with KAP-GFP) and the retrograde motor dynein-1b (with D1bLIC-Cherry) has further revealed significant differences in how these motors are recycled back and forth within a flagellum. Kinesin-II drives anterograde trains in a highly processive fashion and then dissociates from the IFT trains when they reach at the flagellar tip. KAP-GFP then returns to the flagellar base by diffusing within the flagellum, similar to the diffusion of kinesin-1 in mammalian neurons (Blasius et al., 2013) and in contrast to the retrograde transport of kinesin-II observed in other cilia (Signor et al., 1999; Broekhuis et al., 2014; Williams et al., 2014; Prevo et al., 2015, see below). We propose that the diffusion of KAP-GFP represents the movement of the entire heterotrimeric kinesin-II complex because KAP and the kinesin-II motor subunits co-sediment in sucrose density gradients of purified flagella extracts (Cole et al., 1998; Mueller et al., 2005) and neither KAP nor FLA10 accumulate in flagella during inactivation of retrograde transport (Engel et al., 2012; Pedersen et al., 2006; Reck et al., 2016). In certain cases, KAP-GFP appears to diffuse in an oligomeric form. It remains to be studied what holds KAPs together and whether other components of the IFT trains diffuse with KAP clusters after splitting and mixing at the tip.

The retrograde motor dynein-1b is transported to the flagellar tip on anterograde trains (Reck et al., 2016). Because kinesin and dynein motors do not compete against each other in a tug-of-war on anterograde trains (Shih et al., 2013), we concluded that dynein-1b is carried as an inactive motor complex (Toropova et al., 2017; Zhang et al., 2017) and it actively engages with microtubules only when it reaches the flagellar tip (Figure 4c). The average tip resting time of dynein-1b is similar to kinesin-II (Welch's t test, p = 0.05), but the initiation of retrograde transport by dynein-1b does not require departure of kinesin-II motors from the tip, suggesting that these processes are independent from each other.

The dynamic behavior of the IFT motors in *Chlamydomonas* flagella differs from that in other cilia

Several studies have revealed differences in IFT in the cilia and flagella of different organisms (Prevo et al., 2017). First, the microtubule tracks can vary considerably. In *Chlamydomonas*, the axoneme contains nine doublet microtubules, each composed of a complete A-tubule (with 13 protofilaments) and an incomplete B-tubule (with 10 protofilaments). The B-tubule terminates before the A-tubule less than 1 μm from the flagellar tip (Ringo, 1967; Satish Tammana et al., 2013). Recent electron microscopy studies have revealed that anterograde IFT trains are transported primarily on the B-tubule, whereas retrograde IFT trains are transported on the A-tubule (Stepanek and Pigino, 2016). The pausing of IFT particles observed at the flagellar tip in *Chlamydomonas* may therefore reflect not only the time involved in the re-organization of the IFT particles, but also the time required for switching between microtubule tracks.

In other cilia, such as *C. elegans* sensory and mammalian olfactory cilia, the proximal doublet microtubule segment is shorter, and the distal singlet MTs can vary significantly in length (~2.5 μm in *C. elegans* to >100 μm in mouse olfactory cilia). These cilia also employ two different kinesin-II motors for anterograde IFT (Prevo et al., 2015; Snow et al., 2004; Williams et al., 2014). In *C. elegans*, heterotrimeric kinesin-II is concentrated near the basal body region and transports anterograde IFT particles into the proximal doublet segment, where they are gradually handed over to a homodimeric kinesin-II, OSM-3, for transport into the distal singlet segment (Prevo et al., 2015; Snow et al., 2004). Unlike *Chlamydomonas*, both the heterotrimeric and homodimeric kinesin-II motors are recycled to the ciliary base by retrograde IFT, not by diffusion, in these and other metazoan cilia studied to date (Broekhuis et al., 2014; Mijalkovic et al., 2017; Prevo et al., 2015; Signor et al., 1999; Williams et al., 2014).

Another important difference between IFT in *Chlamydomonas* and metazoan cilia is the dynamic behavior of the motors themselves. IFT particles and motors move processively in the *Chlamydomonas* flagellum (Dentler, 2005), with little or no evidence for the frequent pausing and reversal along the axoneme previously described in *C. elegans* or mouse olfactory sensory cilia (Mijalkovic et al., 2017; Prevo et al., 2015). We also did not observe acceleration and deceleration of IFT motors near turnaround zones, nor the instantaneous (<600 ms) reversal of dynein-1b at the ciliary tip described in *C. elegans* (Mijalkovic et al., 2017; Prevo et al., 2015). The reasons for these differences in IFT dynamics and turnover remain unknown, but they may be related to the variations in ciliary structure and organization described above, differential phosphorylation of kinesin-II motors (Liang et al., 2014), posttranslational modification of the microtubule tracks (Stepanek and Pigino, 2016), and other unidentified factors. In addition, both the frequency and speed of IFT is higher in *Chlamydomonas* (Dentler, 2005; Engel et al., 2009, 2012; Iomini et al., 2001; Reck et al., 2016; Snow et al., 2004; Williams et al., 2014; Wingfield et al., 2017) than that measured thus far in metazoan cilia (Li et al., 2015; Yi et al., 2017). This may allow *Chlamydomonas* to rapidly adjust the length of its flagella in response to internal or external stimuli, whereas most cilia in *C. elegans* sensory neurons or mammalian cells do not undergo extensive structural rearrangements once formed.

A model for flagellar length control in *Chlamydomonas*

Cilia and flagella serve as a model system to study how cells precisely control organelle size because they elongate only in one direction. According to the balance point model, flagellar length is set when flagellar assembly and disassembly rates reach equilibrium (Marshall et al., 2005). While the disassembly rate is independent of flagellar length (Kozminski et al., 1995), the assembly rate is determined by the injection of IFT trains (Marshall et al., 2005). The amount of material being transported by these trains to the tip is correlated strongly with the amount of material localized to the flagellar base (Ludington et al., 2013, 2015; Wren et al., 2013), which serves as a loading dock. Previous studies showed that IFT train size and the number of ciliary cargos per train scales inversely with flagellar length (Craft et al., 2015; Engel et al., 2009), consistent with the reduction of the assembly rate as flagella elongate (Marshall et al., 2005). However, it remained unclear which essential component of the IFT machinery limits the assembly of IFT trains at the basal body during elongation.

We propose that dissociation of kinesin-II from IFT trains serves as a negative feedback mechanism to control the assembly rate in *Chlamydomonas* (Ludington et al., 2015). Our results show that the majority of kinesin-II dissociates from IFT trains at the flagellar tip and diffuses within the flagellum. Diffusion leads to a large accumulation of kinesin-II in the flagellum as the flagellum grows longer, while the amount of kinesin-II at the base decreases several-fold. As a result, lower amounts of kinesin-II are available to bring new anterograde IFT trains to the flagellar tip. This may lead to a reduction in the IFT train size and the rate of flagellar assembly as the flagella elongate (Figure 6e,f). Indeed, a recent theoretical study demonstrated that increased diffusion time of kinesin-II in longer flagella can explain the inverse relationship between length and IFT motor recruitment rate (Hendel et al., 2017).

Consistent with this model, previous studies showed that KAP intensity at the basal body correlates with KAP loading on IFT trains and the assembly rate during flagellar regeneration (Ludington et al., 2013). In the temperature-sensitive mutant strain $fla10^{ts}$, inactivation of kinesin-II motility ceases IFT and leads to resorption of the flagellum at a constant rate (Kozminski et al., 1995; Marshall et al., 2005). At intermediate temperatures, flagellar length correlates strongly with the estimated fraction of active kinesin-II motors in $fla10^{ts}$ cells (Marshall and Rosenbaum, 2001), indicating that the amount of active kinesin-II limits flagellar growth. The experiments performed under Li^+ and cycloheximide treatments (Figure 6d) also support the idea that altering the amount of KAP available for the flagellar compartment positively correlates with the flagellar length and that the equilibrium length is set when KAP gets depleted below a certain threshold at the basal body. We note that the KAP intensity at the flagellar base was lower (34-40%) in Li^+ and cycloheximide treated cells than in control cells at equilibrium (p <0.0001, Figure 6d, left). Although the reason for this difference remains unclear, it could be due to a reduction of KAP concentration in the cytoplasm or changes in the flagellar disassembly rate under treatment (Wilson and Lefebvre, 2004).

Unlike kinesin-II, IFT components are rapidly recycled to the cell body by dynein-1b and the amount of these components at the flagellar base remains nearly constant as the flagella elongate. Therefore, the abundance of IFT components and dynein-1b at the flagellar base is not limiting to maintain the length, consistent with previous observations that a small amount of IFT complexes and dynein-1b is sufficient to maintain fully grown flagella (Reck et al., 2016; Wang et al., 2009).

Diffusion is also proposed to play a role in setting the length of bacterial flagella (Renault et al., 2017), long polymers made from a single protein flagellin. Similar to the flagellar length control model originally proposed for *Chlamydomonas* (Levy, 1974), flagellins are injected into the channel of the filament and they diffuse to reach the assembly site at the filament tip, generating a concentration gradient decreasing towards the tip. As the filament elongates, it grows more slowly because it takes longer for the components to reach the tip. In contrast to bacterial flagellin, structural components are carried to the tip by IFT in eukaryotic flagella. In *Chlamydomonas*, we showed that diffusion of kinesin-II from the tip sets a concentration gradient decreasing towards the basal body, and its return to the flagellar base is delayed as the flagella elongate. This delay limits the amount of kinesin-II available for building longer flagella.

Our model is challenged by studies showing that the kinesin-II mutant strains *fla10ts* and *fla3* maintain nearly full-length flagella at permissive temperatures although they accumulate significantly lower amounts of kinesin-II in the flagellar compartment (Kozminski et al., 1995; Mueller et al., 2005; Pedersen et al., 2006). Remarkably, *fla3* cells exhibit slower flagellar regeneration (Mueller et al., 2005), consistent with our prediction that the lower amount of kinesin-II negatively affects the assembly rate. However, a more recent study showed that *fla10ts* flagella contain wild-type levels of kinesin-II at permissive temperatures (Wang et al., 2009). Given these apparent discrepancies, more quantitative approaches will be required to address whether the amount of kinesin-II correlates with flagellar length.

According to the balance-point model, flagella that contain lower amounts of kinesin-II can still maintain nearly full-length if they also have a lower disassembly rate. The studies that reported a reduction in kinesin-II expression in *fla10ts* and *fla3* cells also noted significantly reduced anterograde IFT frequency and IFT particle subunits in flagella (Mueller et al., 2005; Pedersen et al., 2006). This could negatively affect the disassembly rate because IFT is required for efficiently removing certain axonemal precursors (Qin et al., 2004) and resorbing the flagellum prior to mitosis. Indeed, flagellar resorption before mitosis occurs at a faster rate than flagellar disassembly after inactivation of IFT (Marshall et al., 2005; Pan and Snell, 2005).

The mechanisms that control the expression of IFT components after deflagellation, regulate the exchange of material between the basal body and cytoplasm, and load material onto IFT trains must also play a major role in determining the length of flagella. Several studies have shown that IFT components are upregulated and accumulate in large numbers at the flagellar base after deflagellation (Albee et al., 2013; Lefebvre and Rosenbaum, 1986; Stolc et al., 2005). Additionally, a large pool of IFT components in the cytoplasm partially exchanges with the flagellar pool (Buisson et al., 2013; Engel et al., 2009; Wingfield et al., 2017) because cells can grow half-length flagella after deflagellation under complete inhibition of protein synthesis (Rosenbaum et al., 1969). However, molecular cues that govern these processes remain poorly understood and further studies in mutant cell lines that have abnormally long (Nguyen et al., 2005; Tam et al., 2007) or short flagella may provide new insight for the mechanism of flagellar length control.

Materials and Methods

Strains and cell culture

The *pf18 IFT27-GFP* strain was obtained from the Marshall laboratory (University of California San Francisco) after crossing the *IFT27-GFP* transgene into the *pf18* background as previously described (Engel et al., 2009; Qin et al., 2007). The *ift20::IFT20-GFP* strain (Lechtreck et al., 2009) was obtained from the Lechtreck laboratory (University of Georgia). The *fla3::KAP-GFP* (Mueller et al., 2005) and *d1blic::D1bLIC-GFP* (Reck et al., 2016) strains are available from *Chlamydomona*s Resource Center at the University of Minnesota (RRID: **SCR_014960**). The *d1blic*::*D1bLIC-crCherry KAP-GFP* strain was generated as described below. These strains were not authenticated or tested for mycoplasma contamination. Strains were maintained on plates of TAP media containing 1% agar. For light microscopy, vegetative cells were resuspended in liquid TAP media at 22 ºC for 24-48 hours and passaged to fresh liquid TAP before introduction into a flow chamber.

Isolation and characterization of the *d1blic::D1bLIC-crCherry KAP-GFP* strain.

The *D1bLIC-crCherry* construct was generated by subcloning a *Chlamydomonas* codon-optimized version of the Cherry tag into a genomic copy of the *D1bLIC* gene (Reck et al., 2016). The Cherry tag was amplified by PCR from the plasmid pBR9 mCherryCr (Rasala et al., 2013) and inserted into a unique *Asc*I site located in the last exon of *D1bLIC*. The D1bLIC-crCherry construct was linearized with *Bam*HI and co-transformed into *d1blic* (CC-4487) with the selectable marker pSI103 and plated on TAP medium plus 10 µg/ml paromomycin. 960 transformants were picked into TAP media and screened for changes in colony morphology. 84 colonies were further examined by both phase contrast and fluorescence microscopy for rescue of flagellar assembly and expression of Cherry. Isolated flagella from four colonies were analyzed by Western blot for the presence of full-length D1bLIC-Cherry. A single colony was selected for a second round of transformation using the *KAP-GFP* construct (Mueller et al., 2005) and the plasmid pHyg3 (Berthold et al., 2002) and selection on 10 µg/ml of hygromycin B. Two out of 96 transformants were identified as positive for both GFP and Cherry by fluorescence microscopy, and Western blots of isolated flagella confirmed the presence of both D1bLIC-Cherry and KAP-GFP in the rescued strains. Antibodies used included a rat antibody against *Chlamydomonas* KAP (Mueller et al., 2005), a mouse antibody against GFP (Covance, Inc.), a rabbit antibody against *Chlamydomonas* D1bLIC (Perrone et al., 2003), and a rabbit antibody against mCherry (Rockland Immunochemicals).

Drug treatment

0.34 mM Ca^{2+} in TAP media was depleted by adding 0.5 mM EGTA, which resulted in a free Ca^{2+} concentration of 1.5 µM. The concentration of free Ca^{2+} in the assay buffer as a function of added EGTA was calculated from the Chelator program (http://maxchelator.stanford.edu). For drug treatment assays, a final concentration of 100 µM ciliobrevin D was added to the TAP media, and the data was collected 5-10 minutes after the treatment.

For cycloheximide treatment, cells were deflagellated by pH shock and cycloheximide was added to a final concentration of 1.5 µg/ml immediately afterwards. Cells were allowed to regrow flagella for 2 hours before fixation and imaging. For Li^+ treatment, 50 mM LiCl was added to liquid cell suspensions, and cells were incubated for 2 hours before fixation and imaging.

Deflagellation and flagellar regrowth

For imaging the diffusion gradient in live *fla3::KAP-GFP* cells, we deflagellated cells in TAP media using shear force by rapidly pushing them through a 20G1 ½ syringe. Cells regenerating flagella were imaged in the following hour. For imaging the accumulation of GFP signal at the basal body region and in regenerating flagella, fla*3::KAP-GFP* and *IFT20::IFT20-GFP* cells were deflagellated with pH shock by adding 60 µl 0.5 N acetic acid to 1 ml of cells in TAP media, waiting 45 seconds, and adding 60 µl 0.5 N KOH. Cells were fixed 15, 30, 45, 60, and 75 minutes after pH shock. Fixation was done by pipetting 200 µl of liquid TAP cell culture onto a poly-lysine treated coverslip for 1 minute, then gently treating the coverslip with 4% paraformaldehyde in water for 10 min. Afterwards, the coverslip was treated twice with 100% methanol chilled to -20 ℃ for 5 minutes. Coverslips were dipped in water to remove methanol, mounted in a flow chamber with TAP media, and then imaged immediately.

TIR microscopy

A custom-built objective-type TIR fluorescence microscope was set up using a Nikon TiE inverted microscope equipped with a perfect focusing unit, bright-field illumination, and a 100X 1.49 NA PlanApo oil immersion objective (Nikon). 488 nm and 561 nm solid state lasers (Coherent) were used for GFP and crCherry excitation, respectively. The angle of incident light was adjusted lower than the critical angle to illuminate a deeper field (~300 nm) near the coverslip surface. The fluorescent signal was recorded by an Andor iXon 512 x 512 electron-multiplied charge-coupled device (EM-CCD) camera. 1.5x extra magnification was used to obtain an effective pixel size of 106 nm. Data was collected at 10 Hz. Excitation laser beams were controlled by shutters (Uniblitz). Because the CCD image saturates under intense laser illumination of the focused gate beam, shutter timing was synchronized with the camera acquisition by a data acquisition card (NI, USB-6221) to minimize the number of saturated frames in recorded movies. For two-color imaging, GFP and crCherry fluorescence were separated into two channels on a CCD camera using Optosplit II (Cairn). To avoid bleed-through between channels, movies were acquired using time-sharing between the 488 nm and 561 nm laser beams, synchronized with camera acquisition at 60 ms frame time. The effective pixel size was 160 nm.

PhotoGate assays

The PhotoGate system was assembled as previously described (Belyy et al., 2017). Briefly, a 488-nm laser beam was split into two paths using a half-wave plate and a polarizer beamsplitter cube. The first path was used for objective-type TIRF imaging. The second path was focused (2 MW cm^{-2}) to the image plane and steered with a fast piezo-driven mirror (S-330.8SL, Physik Instrumente). The piezo-driven mirror was mounted at a position conjugate to the back-focal plane of the objective to ensure that the tilting of the mirror resulted in pure translation of the focused beam in the image plane. The mirror provided a usable travel range of 30 µm x 30 µm area at the image plane. The mirror's angle was updated via analog output channels of a data acquisition card (NI, USB-6221) and controlled by software custom-written in LabVIEW.

Flagellar orientation of surface adhered cells was visualized by TIRF imaging. Initially, the gate beam was placed at the tip of flagellum and moved along the flagellar orientation to prebleach the distal half of the flagellum. The gate beam was turned off when it was positioned near the base of the flagellum to allow a single fluorescent anterograde train to enter the flagellum. Occasionally (<5%), two anterograde trains overlapped and entered the flagellum

43

simultaneously. The gate beam was then turned on for 0.2 s of every 1 s to bleach other anterograde trains. Under these conditions, less than 1% of anterograde IFT trains moved faster than the cutoff speed (3.0 μm s^{-1}) and were able to escape the gate. Based on the size of the gate beam in the image plane, gating frequency was adjusted for each experiment to keep the escape probability under 0.01. The trajectories of these trains can be distinguished from each other as they move at different speeds along the flagellum. The locations of flagellar tips were determined by brightfield imaging (data not shown). In two-color PhotoGate experiments, the focused 488-nm laser beam was used to bleach both GFP and crCherry, and 488 and 561 beams were used in a time-sharing mode for TIR excitation.

FRAP assays

FRAP assays on the *fla3::*KAP-GFP strain were performed by photobleaching the center part of the flagellum (5 μm in length) for 200 ms at 25 kW cm^{-2} in the epifluorescence mode. The recovery of fluorescence signal in the bleached area was simultaneously monitored by imaging with a 100 W cm^{-2} TIRF excitation. The analysis was performed by measuring the total fluorescence intensity within the bleached area. Fluorescent signal of anterograde transport was manually excluded from the analysis. 13 different recovery traces were used in the MSD analysis. The intensity of each trace was normalized according to the initial and final intensity.

Confocal microscopy

fla3::KAP-GFP and *IFT20::IFT20-GFP* cells were fixed with paraformaldehyde at 15, 30, 45, 60, and 75 min intervals after deflagellation, as described above. The sample was imaged on a Zeiss confocal microscope using 488 nm laser excitation. Images were recorded with 560 nm *z* step, 63 nm pixel size, and 1.58 μs photon collection per pixel. Fluorescence in basal body and flagellum was quantified using ImageJ. The ratio of flagellar to basal-body KAP-GFP fluorescence in confocal images was similar to that of images recorded with TIR excitation, indicating that the fixation protocol did not result in the loss of diffusing KAP-GFP signal from the flagella. We confirmed that fixation did not alter the relative amount of KAP-GFP in the flagellum and the base by comparing the flagellum to base fluorescence ratio in live and fixed *fla3::*KAP-GFP cells.

Data analysis

Anterograde and retrograde trajectories were manually assigned from kymographs. After the arrival of a single anterograde particle at the tip, the departure of fluorescent retrograde trains was determined at single pixel and frame resolution. The tip resting time for each retrograde train was defined as the duration between the arrival of the fluorescent anterograde train and the departure of the retrograde train from the tip. Tip resting time histograms were constructed and fitted to a Gamma function using MATLAB. The Gamma function was defined as $\Gamma(t) = t^{\alpha-1}e^{-\lambda t}$, where α and λ are shape and rate parameters, respectively.

For single particle tracking analysis, the positions of fluorescent spots were determined by fitting the PSFs to a 2D Gaussian. The positions were fitted throughout the movie except at the frames when the gate beam was on or the frames in which the tracked particle overlapped with other fluorophores. The intensity of the fluorescent spots was estimated by the volume of the 2D Gaussian peak. In a typical assay, we adjusted excitation power to achieve 20-nm localization accuracy at 10 Hz image acquisition rate. Individual GFP particles were tracked for 5 s on average before photobleaching and the diffusion constant was obtained by MSD analysis of

individual spots. In certain kymographs, diffusion of individual KAPs within a flagellum could not be resolved due to the diffraction limit.

To determine the distribution of the KAP-GFP background in flagella, anterograde trajectories in kymographs of *fla3::*KAP-GFP cells were manually removed using custom ImageJ plugins. The remaining pixels were averaged over the kymograph's time axis, giving a time-averaged plot of the KAP-GFP background over the flagellum length. The cells were grouped by flagellar length. The background intensity and flagellum length of each cell were normalized. The average background intensity along the length of the flagellum was calculated for each group of cells.

KAP-GFP efflux from the flagellum was calculated using Fick's law. The slope of the KAP-GFP background over the length of a flagellum was multiplied by the diffusion constant ($1.7 \mu m^2 s^{-1}$). To calculate KAP-GFP influx, the KAP-GFP background was subtracted from the kymographs. Then, the average intensity of anterograde trains was multiplied by the train frequency (1.3 trains s^{-1}) to calculate the influx.

GFP photobleaching rate under TIR illumination was estimated by heavily decorating the coverslip surface with eGFP and calculating the rate of decrease in GFP fluorescence. To estimate the live-cell GFP photobleaching rate in *pf18 IFT27-GFP* cells, the fluorescent intensities of 94 anterograde trains from 9 cells were quantified at each time point en route to the flagellar tip. Each train's intensity profile was normalized by the mean intensity. The normalized intensity values were plotted against time and fit to a single exponential decay. The decay constant was used as the photobleaching rate.

Monte Carlo simulations

Monte Carlo simulations were performed to test the effect of limited number of GFPs per train and GFP photobleaching in PhotoGate experiments using the *pf18 IFT27-GFP* strain. Experimentally measured values were used for the velocity and frequency of anterograde and retrograde trains. Simulations assumed that anterograde trains arrive and retrograde trains depart from the tip through a purely stochastic process adding particles to a mixed flagellar tip pool.

We estimated that each anterograde train contains 6 fluorescent GFPs by comparing the fluorescent intensities of anterograde trains in the *pf18 IFT27-GFP* strain to those of KAP-GFP spots in the *fla3::KAP-GFP* strain under the same imaging conditions and calibrating the number of molecules based on previous photobleaching analysis of the *fla3::KAP-GFP* strain (Engel et al., 2009). Each retrograde train was constructed by a random selection of IFT particles available at the tip. Tip intensity measurements revealed that the signal of the IFT complexes located at the tip is approximately three times brighter than an average anterograde train. The photobleaching of GFPs ($0.07 s^{-1}$) under TIR illumination was accounted for in simulations and trains with at least one fluorescent GFP upon leaving the tip were marked detectable.

Simulations were also run to estimate the distribution of diffusing KAP molecules in the flagellum at a steady-state. In these simulations, previously reported values for the anterograde train injection rate (1.3 trains s^{-1}) (Mueller et al., 2005) and the average number of KAP bound to a single anterograde train for each flagellar length (Engel et al., 2009) were used to estimate the number of KAP that arrives at the flagellar tip per second. KAP dissociated from the trains at the tip and immediately started one dimensional diffusion in the flagellum. The resting time of KAP at the tip was insignificant, and was not accounted for. The flagellum was modeled as a 5 - 12 μm long linear grid with spacing defined as the MSD of KAP diffusing at $1.7 \mu m^2 s^{-1}$ (Figure

2.7h) during the time-step of the simulation (5 ms). At every time point, each active molecule had its grid position changed by +1 or -1. The molecules at the extreme terminus of the tip only moved towards the base. The diffusing KAP molecules were perfectly absorbed to the cell body as they arrived at the flagellar base (i.e. perfect sink) and exited the simulation. The simulations were run for 100,000 time points to allow molecules to reach a steady-state. The number of molecules at each grid position was calculated to plot the distribution of KAP molecules diffusing along the length of the flagellum. The total number of KAP was calculated by integrating the number of KAP diffusing along the entire flagellum and KAP on the anterograde trains. This number was compared to a hypothetical scenario that KAP returns to the cell body with active transport. The simulations were run 10 times to calculate the error.

Simulation codes are available on https://github.com/SingleMoleculeAC/IFT-Dynamics.

References

Albee, A.J., Kwan, A.L., Lin, H., Granas, D., Stormo, G.D., and Dutcher, S.K. (2013). Identification of Cilia Genes That Affect Cell-Cycle Progression Using Whole-Genome Transcriptome Analysis in Chlamydomonas reinhardtti. G3; Genes|Genomes|Genetics *3*, 979–991.

Belyy, V., Shih, S.-M., Bandaria, J., Huang, Y., Lawrence, R.E., Zoncu, R., and Yildiz, A. (2017). PhotoGate microscopy to track single molecules in crowded environments. Nat. Commun. *8*, 13978.

Berthold, P., Schmitt, R., and Mages, W. (2002). An engineered Streptomyces hygroscopicus aph 7" gene mediates dominant resistance against hygromycin B in Chlamydomonas reinhardtii. Protist *153*, 401–412.

Blasius, T.L., Reed, N., Slepchenko, B.M., and Verhey, K.J. (2013). Recycling of Kinesin-1 Motors by Diffusion after Transport. PLoS One *8*, 45–49.

Broekhuis, J.R., Verhey, K.J., and Jansen, G. (2014). Regulation of cilium length and intraflagellar transport by the RCK-kinases ICK and MOK in renal epithelial cells. PLoS One *9*.

Brown, J.M., and Witman, G.B. (2014). Cilia and diseases. Bioscience *64*, 1126–1137.

Buisson, J., Chenouard, N., Lagache, T., Blisnick, T., Olivo-Marin, J.-C.J.-C., and Bastin, P. (2013). Intraflagellar transport proteins cycle between the flagellum and its base. J. Cell Sci. *126*, 327–338.

Chien A. (2017). IFT-Dynamics. GitHub. https://github.com/SingleMoleculeAC/IFT-Dynamics. 6409c53.

Cole, D.G., Diener, D.R., Himelblau, A.L., Beech, P.L., Fuster, J.C., and Rosenbaum, J.L. (1998). Chlamydomonas kinesin-II-dependent intraflagellar transport (IFT): IFT particles contain proteins required for ciliary assembly in Caenorhabditis elegans sensory neurons. J. Cell Biol. *141*, 993–1008.

Collingridge, P., Brownlee, C., and Wheeler, G.L. (2013). Compartmentalized calcium signaling in cilia regulates intraflagellar transport. Curr. Biol. *23*, 2311–2318.

Craft, J.M., Harris, J.A., Hyman, S., Kner, P., and Lechtreck, K.F. (2015). Tubulin transport by IFT is upregulated during ciliary growth by a cilium-autonomous mechanism. J. Cell Biol. *208*, 223–237.

Dentler, W. (2005). Intraflagellar transport (IFT) during assembly and disassembly of Chlamydomonas flagella. J. Cell Biol. *170*, 649–659.

Engel, B.D., Ludington, W.B., and Marshall, W.F. (2009). Intraflagellar transport particle size scales inversely with flagellar length: Revisiting the balance-point length control model. J. Cell

Biol. *187*, 81–89.

Engel, B.D., Ishikawa, H., Wemmer, K. a., Geimer, S., Wakabayashi, K.I., Hirono, M., Craige, B., Pazour, G.J., Witman, G.B., Kamiya, R., et al. (2012). The role of retrograde intraflagellar transport in flagellar assembly, maintenance, and function. J. Cell Biol. *199*, 151–167.

Firestone, A.J., Weinger, J.S., Maldonado, M., Barlan, K., Langston, L.D., O'Donnell, M., Gelfand, V.I., Kapoor, T.M., Chen, J.K., O'Donnell, M., et al. (2012). Small-molecule inhibitors of the AAA+ ATPase motor cytoplasmic dynein. Nature *484*, 125–129.

Fujiu, K., Nakayama, Y., Iida, H., Sokabe, M., and Yoshimura, K. (2011). Mechanoreception in motile flagella of Chlamydomonas. Nat. Cell Biol. *13*, 630.

Harris, J.A., Liu, Y., Yang, P., Kner, P., and Lechtreck, K.F. (2016). Single-particle imaging reveals intraflagellar transport-independent transport and accumulation of EB1 in Chlamydomonas flagella. Mol. Biol. Cell *27*, 295–307.

Helenius, J., Brouhard, G., Kalaidzidis, Y., Diez, S., and Howard, J. (2006). The depolymerizing kinesin MCAK uses lattice diffusion to rapidly target microtubule ends. Nature *441*, 115–119.

Hendel, N.L., Thomson, M., and Marshall, W.F. (2017). Diffusion as a ruler: Modeling kinesin diffusion as a length sensor for intraflagellar transport. bioRxiv Prepr.

Iomini, C., Babaev-Khaimov, V., Sassaroli, M., and Piperno, G. (2001). Protein particles in Chlamydomonas flagella undergo a transport cycle consisting of four phases. J. Cell Biol. *153*, 13–24.

Ishikawa, H., and Marshall, W.F. (2011). Ciliogenesis: building the cell's antenna. Nat Rev Mol Cell Biol *12*, 222–234.

Kozminski, K.G., Johnson, K. a, Forscher, P., and Rosenbaum, J.L. (1993). A motility in the eukaryotic flagellum unrelated to flagellar beating. Proc. Natl. Acad. Sci. U. S. A. *90*, 5519–5523.

Kozminski, K.G., Beech, P.L., and Rosenbaum, J.L. (1995). The Chlamydomonas kinesin-like protein FLA10 is involved in motility associated with the flagellar membrane. J. Cell Biol. *131*, 1517–1527.

Laib, J.A., Marin, J.A., Bloodgood, R.A., and Guilford, W.H. (2009). The reciprocal coordination and mechanics of molecular motors in living cells. Proc Natl Acad Sci U S A *106*, 3190–3195.

Lechtreck, K.-F., Johnson, E.C., Sakai, T., Cochran, D., Ballif, B. a, Rush, J., Pazour, G.J., Ikebe, M., and Witman, G.B. (2009). The Chlamydomonas reinhardtii BBSome is an IFT cargo required for export of specific signaling proteins from flagella. J. Cell Biol. *187*, 1117–1132.

Lechtreck, K.F., Van De Weghe, J.C., Harris, J.A., and Liu, P. (2017). Protein transport in growing and steady-state cilia. Traffic.

Lefebvre, P. a, and Rosenbaum, J.L. (1986). Regulation of the synthesis and assembly of ciliary and flagellar proteins during regeneration. Annu. Rev. Cell Biol. *2*, 517–546.

Levy, E.M. (1974). Flagellar elongation as a moving boundary problem. Bull. Math. Biol. *36*, 265–273.

Li, W., Yi, P., and Ou, G. (2015). Somatic CRISPR-Cas9-induced mutations reveal roles of embryonically essential dynein chains in Caenorhabditis elegans cilia. J. Cell Biol. *208*, 683–692.

Liang, Y., Pang, Y., Wu, Q., Hu, Z., Han, X., Xu, Y., Deng, H., and Pan, J. (2014). FLA8/KIF3B Phosphorylation Regulates Kinesin-II Interaction with IFT-B to Control IFT Entry and Turnaround. Dev. Cell *30*, 585–597.

Ludington, W.B., Wemmer, K. a, Lechtreck, K.F., Witman, G.B., and Marshall, W.F. (2013). Avalanche-like behavior in ciliary import. Proc. Natl. Acad. Sci. U. S. A. *110*, 3925–3930.

Ludington, W.B., Ishikawa, H., Serebrenik, Y. V., Ritter, A., Hernandez-Lopez, R.A., Gunzenhauser, J., Kannegaard, E., and Marshall, W.F. (2015). A systematic comparison of mathematical models for inherent measurement of ciliary length: How a cell can measure length and volume. Biophys. J. *108*, 1361–1379.

Marshall, W.F., and Rosenbaum, J.L. (2001). Intraflagellar transport balances continuous turnover of outer doublet microtubules: implications for flagellar length control. J. Cell Biol. *155*, 405–414.

Marshall, W., Qin, H., Brenni, M., and Rosenbaum, J. (2005). Flagellar Length Control System: Testing a Simple Model Based on Intraflagellar Transport and Turnover. Mol. Biol. Cell *16*, 270–278.

Mijalkovic, J., Prevo, B., Oswald, F., Mangeol, P., and Peterman, E.J.G. (2017). Ensemble and single-molecule dynamics of IFT dynein in Caenorhabditis elegans cilia. Nat. Commun. *8*, 14591.

Morga, B., and Bastin, P. (2013). Getting to the heart of intraflagellar transport using Trypanosoma and Chlamydomonas models : the strength is in their differences

Mueller, J., Perrone, C.A., Bower, R., Cole, D.G., and Porter, M.E. (2005). The FLA3 KAP Subunit Is Required for Localization of Kinesin-2 to the Site of Flagellar Assembly and Processive Anterograde Intraflagellar Transport. Mol. Biol. Cell *16*, 1341–1354.

Nachury, M. V, and Mick, D.U. (2019). Establishing and regulating the composition of cilia for signal transduction. Nat. Rev. Mol. Cell Biol.

Nakamura, S., Takino, H., and Kojima, M.K. (1987). Effect of Lithium on Flagellar Length in Chlamydomonas reinhardtii. Cell Struct. Funct. *12*, 369–374.

Nguyen, R.L., Tam, L.W., and Lefebvre, P.A. (2005). The LF1 gene of Chlamydomonas reinhardtii encodes a novel protein required for flagellar length control. Genetics *169*, 1415–1424.

Pan, J., and Snell, W.J. (2005). Chlamydomonas shortens its flagella by activating axonemal disassembly, stimulating IFT particle trafficking, and blocking anterograde cargo loading. Dev. Cell *9*, 431–438.

Pazour, G.J., Dickert, B.L., and Witman, G.B. (1999). The DHC1b (DHC2) isoform of cytoplasmic dynein is required for flagellar assembly. J Cell Biol *144*, 473–481.

Pedersen, L.B., Geimer, S., and Rosenbaum, J.L. (2006). Dissecting the molecular mechanisms of intraflagellar transport in Chlamydomonas. Curr. Biol. *16*, 450–459.

Perrone, C.A., Tritschler, D., Patrick, T., Raqual, B., Yoder, B.K., and Porter, M.E. (2003). A Novel Dynein Light Intermediate Chain Colocalizes with the Retrograde Motor for Intraflagellar Transport at Sites of Axoneme Assembly in Chlamydomonas and Mammalian Cells. Mol. Biol. Cell *14*, 2559–2569.

Pigino, G., Geimer, S., Lanzavecchia, S., Paccagnini, E., Cantele, F., Diener, D.R., Rosenbaum, J.L., and Lupetti, P. (2009). Electron-tomographic analysis of intraflagellar transport particle trains in situ. J. Cell Biol. *187*, 135–148.

Porter, M.E., Bower, R., Knott, J.A., Byrd, P., and Dentler, W. (1999). Cytoplasmic dynein heavy chain 1b is required for flagellar assembly in Chlamydomonas. Mol. Biol. Cell *10*, 693–712.

Prevo, B., Mangeol, P., Oswald, F., Scholey, J.M., and Peterman, E.J.G. (2015). Functional differentiation of cooperating kinesin-2 motors orchestrates cargo import and transport in *C. elegans* cilia. Nat. Cell Biol. *17*, 1536–1545.

Prevo, B., Scholey, J.M., and Peterman, E.J.G. (2017). Intraflagellar transport: Mechanisms of motor action, cooperation, and cargo delivery. FEBS J.

Qin, H., Diener, D.R., Geimer, S., Cole, D.G., and Rosenbaum, J.L. (2004). Intraflagellar transport (IFT) cargo: IFT transports flagellar precursors to the tip and turnover products to the cell body. J. Cell Biol. *164*, 255–266.

Qin, H., Wang, Z., Diener, D., Rosenbaum, J., Hongmin Qin, Zhaohui Wang, Dennis Diener, and J.R., Qin, H., Wang, Z., Diener, D., and Rosenbaum, J. (2007). Intraflagellar Transport Protein 27 Is a Small G Protein Involved in Cell-Cycle Control. Curr. Biol. *17*, 193–202.

Rasala, B.A., Barrera, D.J., Ng, J., Plucinak, T.M., Rosenberg, J.N., Weeks, D.P., Oyler, G.A.,

Peterson, T.C., Haerizadeh, F., and Mayfield, S.P. (2013). Expanding the spectral palette of fluorescent proteins for the green microalga Chlamydomonas reinhardtii. Plant J. *74*, 545–556.

Reck, J., Schauer, A.M., VanderWaal Mills, K., Bower, R., Tritschler, D., Perrone, C.A., and Porter, M.E. (2016). The role of the dynein light intermediate chain in retrograde IFT and flagellar function in Chlamydomonas. Mol. Biol. Cell *27*, 2404–2422.

Renault, T.T., Abraham, A.O., Bergmiller, T., Paradis, G., Rainville, S., Charpentier, E., Guet, C.C., Tu, Y., Namba, K., Keener, J.P., et al. (2017). Bacterial flagella grow through an injection-diffusion mechanism. Elife *6*, e23136.

Ringo, D.L. (1967). Flagellar motion and fine structure of the flagellar apparatus in Chlamydomonas. J. Cell Biol. 543–571.

Rompolas, P., Pedersen, L.B., Patel-King, R.S., and King, S.M. (2007). Chlamydomonas FAP133 is a dynein intermediate chain associated with the retrograde intraflagellar transport motor. J Cell Sci *120*, 3653–3665.

Rosenbaum, J.L., Moulder, J.E., and Ringo, D.L. (1969). Flagellar elongation and shortening in Chlamydomonas. The use of cycloheximide and colchicine to study the synthesis and assembly of flagellar proteins. J. Cell Biol. *41*, 600–619.

Satir, P., Pedersen, L.B., and Christensen, S.T. (2010). The primary cilium at a glance. J. Cell Sci. *123*, 499–503.

Satish Tammana, T. V, Tammana, D., Diener, D.R., Rosenbaum, J., Tammana, T.V.S., Tammana, D., Diener, D.R., and Rosenbaum, J. (2013). Centrosomal protein CEP104 (Chlamydomonas FAP256) moves to the ciliary tip during ciliary assembly. J. Cell Sci. *126*, 5018–5029.

Shih, S.M., Engel, B.D., Kocabas, F., Bilyard, T., Gennerich, A., Marshall, W.F., and Yildiz, A. (2013). Intraflagellar transport drives flagellar surface motility. Elife *2*, e00744.

Signor, D., Wedatman, K.P., Orozco, J.T., Dwyer, N.D., Bargmann, C.I., Rose, L.S., and Scholey, J.M. (1999). Role of a class DHC1b dynein in retrograde transport of IFT motors and IFT raft particles along cilia, but not dendrites, in chemosensory neurons of living Caenorhabditis elegans. J. Cell Biol. *147*, 519–530.

Silflow, C.D., and Lefebvre, P.A. (2001). Assembly and Motility of Eukaryotic Cilia and Flagella. Lessons from Chlamydomonas reinhardtii; Plant Physiol. *127*, 1500 LP – 1507.

Snow, J.J., Ou, G., Gunnarson, A.L., Walker, M.R.S., Zhou, H.M., Brust-Mascher, I., and Scholey, J.M. (2004). Two anterograde intraflagellar transport motors cooperate to build sensory cilia on C. elegans neurons. Nat. Cell Biol. *6*, 1109–1113.

Stepanek, L., and Pigino, G. (2016). Microtubule doublets are double-track railways for intraflagellar transport trains. Science *352*, 721–724.

Stolc, V., Samanta, M.P., Tongprasit, W., and Marshall, W.F. (2005). Genome-wide transcriptional analysis of flagellar regeneration in Chlamydomonas reinhardtii identifies orthologs of ciliary disease genes. Proc Natl Acad Sci U S A *102*, 3703–3707.

Taschner, M., and Lorentzen, E. (2019). The Intraflagellar Transport Machinery.

Tam, L.W., Wilson, N.F., and Lefebvre, P.A. (2007). A CDK-related kinase regulates the length and assembly of flagella in Chlamydomonas. J. Cell Biol. *176*, 819–829.

Toropova, K., Mladenov, M., and Roberts, A.J. (2017). Intraflagellar transport dynein is autoinhibited by trapping of its mechanical and track-binding elementsToropova, K., Mladenov, M., & Roberts, A. J. (2017). Intraflagellar transport dynein is autoinhibited by trapping of its mechanical and track-binding . Nat. Struct. Mol. Biol. *56*, 1–6.

Viswanadha, R., Sale, W.S., and Porter, M.E. (2019). Ciliary Motility : Regulation of Axonemal Dynein Motors.

Wang, Z., Fan, Z.C., Williamson, S.M., and Qin, H. (2009). Intraflagellar transport (IFT) protein IFT25 is a phosphoprotein component of IFT complex B and physically interacts with IFT27 in Chlamydomonas. PLoS One *4*.

Williams, C.L., McIntyre, J.C., Norris, S.R., Jenkins, P.M., Zhang, L., Pei, Q., Verhey, K., and Martens, J.R. (2014). Direct evidence for BBSome-associated intraflagellar transport reveals distinct properties of native mammalian cilia. Nat. Commun. *5*, 5813.

Wilson, N.F., and Lefebvre, P. a (2004). Regulation of Flagellar Assembly by Glycogen Synthase Kinase 3 in Chlamydomonas reinhardtii Regulation of Flagellar Assembly by Glycogen Synthase Kinase 3 in Chlamydomonas reinhardtii. Eukaryot. Cell *3*, 1307–1319.

Wingfield, J.L., Mengoni, I., Bomberger, H., Jiang, Y.Y., Walsh, J.D., Brown, J.M., Picariello, T., Cochran, D.A., Zhu, B., Pan, J., et al. (2017). IFT trains in different stages of assembly queue at the ciliary base for consecutive release into the cilium. Elife *6*, 1–27.

Wren, K.N., Craft, J.M., Tritschler, D., Schauer, A., Patel, D.K., Smith, E.F., Porter, M.E., Kner, P., and Lechtreck, K.F. (2013). A differential cargo-loading model of ciliary length regulation by IFT. Curr. Biol. *23*, 2463–2471.

Yang, P., Diener, D.R., Yang, C., Kohno, T., Pazour, G.J., Dienes, J.M., Agrin, N.S., King, S.M., Sale, W.S., Kamiya, R., et al. (2006). Radial spoke proteins of Chlamydomonas flagella. J. Cell Sci. *119*, 1165 LP – 1174.

Yi, P., Li, W.J., Dong, M.Q., and Ou, G. (2017). Dynein-Driven Retrograde Intraflagellar Transport Is Triphasic in C. elegans Sensory Cilia. Curr. Biol. *27*, 1448–1461.e7.

Zhang, K., Foster, H.E., Rondelet, A., Lacey, S.E., Bahi-Buisson, N., Bird, A.W., and Carter, A.P. (2017). Cryo-EM Reveals How Human Cytoplasmic Dynein Is Auto-inhibited and Activated. Cell *169*, 1303–1314.e18.

Acknowledgments

Video Resources:

Because most of my work has been live-cell imaging of moving protein complexes, I believe that watching movies from our microscopes is the best way of understanding our assays. Therefore, I attached videos to this thesis as supplementary media.

They are also available in our ELife manuscript, which can be found at:
https://elifesciences.org/articles/28606

Video Legends

Video 1. Tracking of individual IFT trains in *Chlamydomonas*. IFT movement was visualized by TIR imaging of a surface-adhered *pf18 IFT27-GFP* cell. Green and blue arrows represent the cell body and flagellar tips, respectively. The size of the window is 15.5 × 27.6 μm. The movie was recorded at 10 frames s^{-1} and is played in real time. This video corresponds to Figure 2.1a.

Video 2. Observing the dynamics of single IFT trains at the flagellar tip using the PhotoGate. The distal half of the flagellum on the right of a surface-adhered *pf18 IFT27-GFP* cell is photobleached by an intense laser beam. The gate beam is turned off to allow a single anterograde train to enter the bleached region and turned on repeatedly at the base of the flagellum to bleach the subsequent anterograde trains. Two retrograde trains emanate from a single fluorescent anterograde train at the tip. Frames with the gate beam on are removed for illustration purposes. The movie was recorded at 10 frames s^{-1} and is played in real time. Cyan and magenta arrows represent anterograde and retrograde particles, respectively. Pre-bleaching frames are marked by red borders. The position of the PhotoGate is marked by a red line. This video corresponds to Figure 2.1c.

Video 3. Tip return dynamics of two fluorescent anterograde trains using the PhotoGate. A flagellum of a surface-adhered *pf18 IFT27-GFP* cell is photobleached. Two fluorescent anterograde IFT trains are allowed pass through the gate without photobleaching and subsequent anterograde trains were photobleached by the gate beam. After the anterograde trains reach the tip, three retrograde trains return with fluorescent signal from these trains. The movie was recorded at 10 frames s^{-1} and is played in real time. Cyan and magenta arrows represent anterograde and retrograde particles, respectively. The position of the PhotoGate is marked by a red line. This video corresponds to Figure 2.1d.

Video 4. Tip return dynamics of three fluorescent anterograde trains using the PhotoGate. A flagellum of a surface-adhered *pf18 IFT27-GFP* cell is photobleached. Three fluorescent anterograde IFT trains are allowed pass through the gate without photobleaching and subsequent anterograde trains were photobleached by the gate beam. The frames in which the gate beam was on were deleted for illustration purposes. After the anterograde trains reach the tip, four retrograde trains return with fluorescent signal from these trains. The movie was recorded at 10 frames s^{-1} and is played in real time. Cyan and magenta arrows represent anterograde and retrograde particles, respectively. Pre-bleaching frames are marked by red borders. The position of the PhotoGate is marked by a red line. This video corresponds to Figure 2.1e.

Video 5. Tip return dynamics of D1bLIC-GFP. In a surface-adhered *d1blic::D1bLIC-GFP* cell, one D1bLIC-GFP particle is allowed to pass through the gate without photobleaching and two fluorescent retrograde particles return to the base. The movie was recorded at 10 frames s^{-1}

and is played in real time. Cyan and magenta arrows represent anterograde and retrograde particles, respectively. Pre-bleaching frames are marked by red borders. The position of the PhotoGate is marked by a red line. This video corresponds to Figure 2.7c.

Video 6. KAP-GFP dissociates from IFT trains at the tip. In the *fla3::KAP-GFP* strain, one fluorescent KAP-GFP particle is allowed to pass through the gate without photobleaching. The KAP-GFP particle undergoes diffusive motion after arriving at the flagellar tip. The size of the window is 26.6×16.6 μm. The movie was recorded at 10 frames s^{-1} and is played in real time. Cyan and magenta arrows represent anterograde and diffusing particles, respectively. The position of the PhotoGate is marked by a red line. This video corresponds to Figure 2.7f.

Video 7. Diffusing KAP-GFP particles can break apart after leaving the tip. In the *fla3::KAP-GFP* strain, one fluorescent KAP-GFP particle is allowed to pass through the gate without photobleaching. The KAP-GFP particle undergoes diffusive motion after arriving at the flagellar tip. While diffusing, the particle breaks further into smaller KAP particles. The size of the window is 30.2×31.1 μm. The movie was recorded at 10 frames s^{-1} and is played in real time. Cyan and magenta arrows represent anterograde and diffusing particles, respectively. The position of the PhotoGate is marked by a red line. This video corresponds to Figure 2.9.

Video 8. Dual color imaging of KAP-GFP and D1bLIC-crCherry. The movements of KAP-GFP and D1bLIC-crCherry are simultaneously tracked in a surface-adhered *d1blic::D1bLIC-crCherry KAP-GFP* cell. KAP and D1bLIC co-localize in the anterograde direction. D1bLIC displays retrograde tracks while retrograde transport of KAP is rarely seen. KAP-GFP channel is on the left and D1bLIC-crCherry channel is on the right. The movie was recorded at 8.3 frames s^{-1} and is played in real time. This video corresponds to Figure 3.1a.

Video 9. Recovery of KAP-GFP after photobleaching the middle section of a flagellum. A surface-adhered *fla3::KAP-GFP* is imaged under TIRF illumination. The middle part of the flagellum is bleached by a 25 kW cm^{-2} laser beam for 0.1 s and the cell is imaged under 100 W cm^{-2} TIRF excitation. The fluorescent signal recovers with different kinetics from each side of the flagellum. The data was collected at 10 frames s^{-1} and is played in real time. Green and blue arrows represent the cell body and flagellar tips, respectively. The photobleached area is marked by thin red lines. This video corresponds to Figure 3.4a.

Further directions

There are several possible extensions of the work I've presented in this dissertation. I will briefly mention two possible directions as logical next steps.

Determining the tip dynamics and interplay of IFT complex A and complex B proteins using multi-color PhotoGate experiments
The non-motor, non-cargo proteins that make up IFT trains have historically been divided into 2 complexes, IFT-A and IFT-B based on how they co-purify. Recently, electron microscopy work has shown that IFTA and IFTB proteins exist in a 1:2 stoichiometry on single anterograde IFT trains. (Jordan et al. 2018) It is unknown how A and B complex proteins differentially remodel at the ciliary tip during the transition from anterograde to retrograde movement.

In this work, we analyzed the tip dynamics of IFT27-GFP, an IFT-B complex protein. In more recent years, other groups have fluorescently tagged IFT-A proteins in *Chlamydomonas*, creating opportunities for a similar analysis of these proteins.

We also used the PhotoGate to simultaneously image the behavior of kinesin-2 and dynein-1b motors at the flagellar tip. We concluded that the two motors exit the tip independently of each other. A strain of *Chlamydomonas* with IFT-A and IFT-B proteins orthogonally fluorescently labelled would enable a similar analysis of the two genres of structural IFT proteins. Moreover, other labelling permutations of motor and structural IFT components could show some other tip remodeling interactions.

Testing kinesin-2's effect on flagellar length control
Our model of flagellar length control provides correlative evidence that kinesin-2 can become limiting as the flagellum grows longer, and therefore may be responsible for slower flagellar assembly rates in long flagella.

One direct test of this theory would be to reduce the amount of kinesin-2 available to the flagellum. If flagellar length correlates to the amount of available kinesin-2, this could provide strong evidence that kinesin-2 becomes limiting. One way of doing this would be to perform RNAi on kinesin-2 and quantify the amount of knockdown using Western blotting. A comparable experiment was performed by Wallace Marshall, in which he observed a *Chlamydomonas* mutant harboring a point mutation in a kinesin-2 subunit that rendered the motor inactive at a "restrictive" temperature. He observed that the flagellar length of these mutants at intermediate temperatures were somewhere between full-length and completely restricted, with lower temperatures leading to longer flagella. However, this did not directly show that the amount of available active kinesin-2 was responsible for flagellar length.

It is also possible to test this model by reducing the diffusion constant of kinesin-2, allowing it to be sequestered in longer flagellum to different extents. If diffusion is rate limiting for flagellar elongation, slower-diffusing kinesin-2 would remain in flagella longer, and therefore cause shorter equilibrium-length flagella.